UNIVERSITATEA VALAHIA DIN TÂRGOVIȘTE
SAPIENTIA ET VIRTUS
1992

sciendo

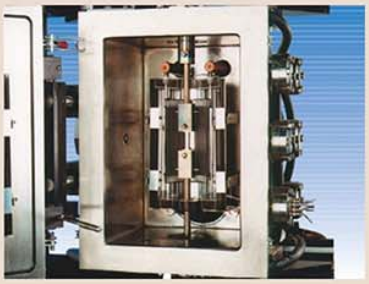

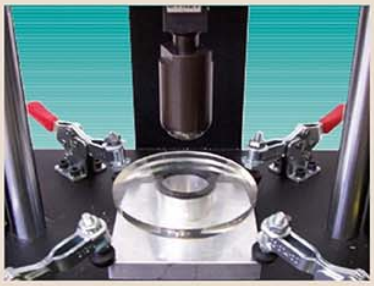

The Scientific Bulletin of Valahia University MATERIALS and MECHANICS

2018

Vol. 16 No. 15

The Scientific Bulletin of VALAHIA University
MATERIALS and MECHANICS –Vol. 16, No. 15

DOI 10.1515/bsmm-2018-0011

CONCRETES WITH ORGANIC ADMIXTURES

Nicolae ANGELESCU, Dan Nicolae UNGUREANU, Vasile BRATU

Valahia University of Targoviste, Faculty of Materials Engineering and Mechanics,
13 Aleea Sinaia Street, Targoviste, Romania

E-mail: danungureanu2002@yahoo.com

Abstract: *The current work is intended to explain the role of some organic admixtures on the hardened structure of refractory concretes with aluminous cement. The influences on the mechanical-structural properties in the normal hardening but in the heating conditions at different temperatures are emphasized, also. These are due to the influence on the hydration process (i.e. the kind of the neoformations and degree of hydration) and implicitly on the size and distribution of structural pores.*

***Keywords*:** refractory concretes, organic admixtures, strengths, distributive porosity.

1. INTRODUCTION

Obtaining refractory materials with concretes qualities and having properties similar to those of high quality burnt shaped products is a frequent and up-to-date preoccupation [1-12].

That is why this paper intends to examine the way of obtaining refractory concretes with this type of properties, having a lower aluminous cement content and using calcium lignosulphonate (LSC), melamine and naphthalene formaldehyde type substances (VIMC11 and VIMC22, respectively) as admixtures.

Also, it is studied the mentioned admixtures action on concrete hardening as well as mechano-structural properties of obtained concretes.

2. EXPERIMETAL CONDITIONS

Concretes with a varying dosage of aluminous cement type CA + CA_2 ($CaO{\cdot}Al_2O_3$ + $CaO{\cdot}2Al_2O_3$) and tabular alumina aggregate (granulation max. 3.36 mm), with and without admixtures, were studied.

Granulometry of the aggregate were calculated according to the Bollomey curve. Mechanical strength, porosity and refractoriness of the concretes were determined, also. BET specific surface of hydrated cement was measured and diffractometry analyses were carried out. The physic-mechanical and texture properties were examined on concrete samples subjected to drying and heat treatment after 3 days of free hardening. Determination of the specific surface and diffractometric analyses were carried out on the hydrated cement pastes, with or without admixtures – for the optimum proportion of additive.

3. RESULTS AND DISCUTION

Lowering the cement dosage to obtain highly refractory concretes (prepared with the high quality aggregate), without using admixtures is far to being the best solution since, under such circumstances, the structure obtained have a much lower mechanical strength.

Using admixtures in the properly chosen proportions may help to obtain concretes with improved mechanical properties, keeping the advantage of increasing refractoriness implied by the decrease in cement dosage. The main reason for the effects brought about by the use of admixtures are the morphological modifications and, as result, the structural-textural ones, appearing during the hardening process of aluminous cements and, implicitly, of the corresponding concretes.

These modifications have to be correlated with the effects found in the fresh mixture properties and in the cement and water interactions kinetics, also. It was found possible to determine an optimal proportion of additives, considered from the point of view of the overall effect of the development of the structural-mechanical properties, on the condition that the obvious advantages implied by the use of a low cement dosage (especially the increase of concrete refractoriness) to be maintained.

Cement hydration diffractometric analyses - with or without admixtures – for the optimum proportion of additive (determined by detailed testing) – points out the existence of a larger proportion of gel hydrating neoformations; the intensity of crystalline hydration products characteristic lines, in the case of samples with admixtures, is lower against a more intensive radiation background – fig. 1.

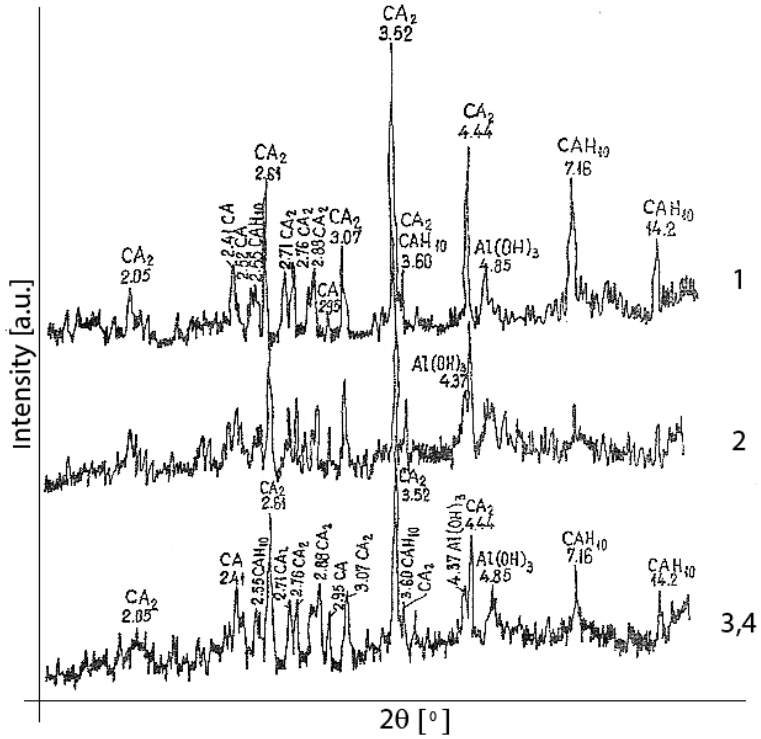

Figure 1. Diffractograms of aluminous cements hydrated for 3 days: 1. Non-additivated cement; 2. Cement with LSC, ad/c = 0.001; 3. Cement with VIMC11, ad/c = 0.0016; 4. Cement with VIMC22, ad/c = 0.0045.

For the same hydration interval, the additivated hydrated cements have a higher or even much higher degree of dispersion, although the degree of cement hydration is somewhat lower or even much lower. LSC especially, has, in the context, an obvious retarding effect (Table 1).

Table 1. BET specific surface and hydration degree of cement with or without admixture, after 3 days of hardening

Cement sample	Admixture	Ad/c ratio*)	BET specific surface, m^2/g	Degree of hydration, %	
				CA	CA_2
$CA + CA_2$	None	-	2.524	65.01	21.08
$CA + CA_2$	LSC	0.0010	3.094	56.05	17.65
$CA + CA_2$	VIMC11	0.0016	3.536	64.92	20.65
$CA + CA_2$	VIMC22	0.0045	5.666	57.15	20.92

*) Admixture/cement ratio

Although all admixtures acted as hardening retarding agents, the mechanical strengths and the porosities obtained after 3 days of hardening using the optimum addition ratio, were improved in all cases; the higher mechanical resistances and the lower porosities of the concretes with admixtures remain the same even when heat treated at high temperatures, Table 2.

This behavior is the result of the admixtures positive influence on hydrated cement dispersion, when the water proportion is somewhat lower than that used in standard concretes. It can thus be seen that concretes with admixtures, with 12.5% cement have a better behavior from the mechanical point of view, even than concretes with 20% cement, but without additives, having an obviously lower porosity even when heat treated.

Concretes with only 5% cement content, besides the fact that they have lower porosities than concretes without admixtures, develop strengths somehow equivalent to those of concrete with 12.5% cement nonadditivated to about 1000^0C; at higher temperatures, the strengths are superior even to concretes free additives with 20% cement. With all of those, one should add the increase of refractoriness.

The admixtures type VIMC22 has the best effect on porosity decrease, among the studied additives (with the obvious displacement of pore size towards lower values – fig. 2), as well as with regard to improvement in mechanical resistance.

Table 2. Mechano-structural properties of CA + CA_2 cement concretes and tabular alumina as aggregate, additivated or nonadditivated in optimum proportion *

Heating temperature after 3 days of free hardening, °C	S_f, N/cm²	S_c, N/cm²	P, %	S_f, N/cm²	S_c, N/cm²	P, %	S_f, N/cm²	S_c, N/cm²	P, %	S_f, N/cm²	S_c, N/cm²	P, %
	Concretes with 20% cement, nonadditivated			Concretes with 12,5% cement, nonadditivated			Concretes with 5% cement, nonadditivated			Concretes with 5% cement and LSC, ad/c = 0.001		
110	750	2380	28	640	2000	26	230	1380	25	310	1770	23
400	800	2120	32	400	1820	28	220	1150	26	230	1460	24
600	530	1980	33	360	1660	30	190	1100	26	190	1440	25
800	440	1880	34	310	1500	30	130	900	26	190	1260	25
1000	340	1320	37	200	940	31	100	700	27	150	1000	26
1200	300	1300	37	200	900	32	100	750	27	200	1080	26
1300	260	1250	37	250	1050	33	11	800	27	360	1550	25
1500	990	3000	28	760	1980	28	600	1900	-	850	2440	24
1700	-	1900	37	800	1600	34	650	1920	26	930	2440	25
Refractoriness	1820°C			1860°C			⩾1890°C			⩾1890°C		
	Concretes with 12.5% cement and LSC, ad/c = 0.001			Concretes with 5% cement and VIMC22, ad/c = 0.0045			Concretes with 12.5% cement and VIMC22, ad/c = 0.0045			Concretes with 12.5% cement and VIMC11, ad/c = 0.0016		
110	890	3750	23	420	2200	22	1060	4000	24	740	3400	25
400	720	3450	25	340	1800	23	880	3380	26	720	2840	26
600	640	3250	26	250	1710	24	630	3060	28	700	2700	28
800	480	2500	26	210	1500	25	540	2650	30	510	2300	30
1000	310	1730	28	180	1420	26	610	2560	30	460	1710	30
1200	280	1420	29	200	1560	26	470	176	31	420	1400	31
1300	670	1970	29	400	1980	25	500	220	28	420	1640	29
1500	1410	3670	26	760	2610	23	1360	3800	28	1050	3350	29
1700	1030	2360	34	1060	2720	24	1300	3700	30	1000	3200	31
Refractoriness	1860°C			⩾1890°C			1860°C			1860°C		

*) S_f = Flexural strength; S_c = Compressive strength; P = Porosity.

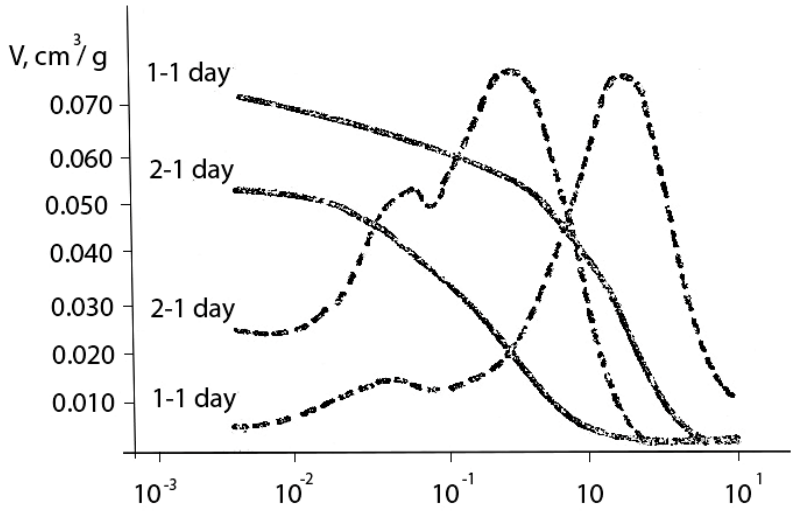

Figure 2. Distributive porosity of refractory concretes without or with VIMC22 (_____ integral curves, - - - - - differential curves)

4. CONCLUSIONS

The result of the present research work leads to the following conclusions:

- the organic admixtures have a positive influence on refractory concretes textural-mechanical characteristics, especially by their dispersed action on hydrated cements.

- the positive influence of the admixtures is achieved on the condition that they are used according to certain optimum values for the additive/cement ratio, taking into account the correlation between the proportion of the admixtures and their effect as a dispersing and hardening retarding agent.

- the organic additives have a positive influence, as a result of the modifications induced in the texture of the concrete`s matrix and their behavior at high temperatures even within the critical temperature range.

- the presence of admixtures in concretes makes a decrease in the cement dosage possible, with an increase in refractoriness and decrease in porosity, and with no negative influence on mechanical properties.

REFERENCES

[1] N. Angelescu – Betoane cu dozaj redus de ciment. Doctorate thesis, Politehnica University, Bucharest, 1983.

[2] B. K. Carr – Refractories Journal (1975), 12, 5-6.

[3] L. Prost – L`ind. Ceram (1963), 661, 279.

[4] I. Teoreanu, N. Angelescu – Mat. Constr. 8 (1978), 3, 127.

[5] I. Teoreanu, N. Angelescu – Mat. Constr. 10 (1980), 1, 31.

[6] N. Angelescu – Cement and Concrete World, vol. 8, no. 44, pp. 52-59, 2003, ISSN 1301-0859.

[7] N. Angelescu – Lignosulfonatul de calciu – adaos pentru imbunatatire lucrabilitatii refractarelor monolitice speciale/Calcium Lignosulphonate Addition for Improving Special Monolithic Refractories Workability. Cercetari Metalurgice şi de Noi Materiale – Metallurgy and New Materials Researches (ROMANIA), ISSN 1221-5503, Vol X, nr. 4, pp. 15-25, 2002.

[8] I. Teoreanu, N. Angelescu - The Influence of Some Organic Additives on Refractory Aluminous Cement Hydration. Il Cemento (Italia), vol. 83, pp. 191-198, 1986.

[9] D. Stanciu, I. Ion, J. A. Barosso, N. Angelescu - Self–Compacting Concrete. A Comparison between the Workability Properties**,** Density, Porosity and Mechanical Properties. Metalurgia International, Vol. XVIII(3), p. 138-141, 2013.

[10] I. Ion, J. A. Barosso, N. Angelescu D. Stanciu - Properties of polymer modified concrete in fresh and hardened state**.** Advanced Materials Research, Trans. Tech. Publications, Switzerland, Vols. *687*, pp *204-212*, 2013. Lucrare prezentata la 14th ICPIC International Congresses on Polymers in Concrete, Shanghai (China), 2013.

[11] Angelescu, N**.,** Ionita, C., Bratu, V. - Structural and mechanical characterization of high alumina additivated cement based on high refractory mineralogical compounds. Construction Materials and Structures. Pages 113 – 120. Edited by Ekolu, S,O., Dundu, M., Gao, X., IOS Press, 2014, doi: 10.3233/978-1-61499-466-4-113. Conference: 1st International Conference on Construction Materials and Structures, Johannesburg, South Africa, November 24 – 26, 2014.

[12] Angelescu, N., Ion, I., Stanciu, D., Barosso, J. A., Abdelgader, H. S., Bratu, V. - Role of superplasticizer additives upon hydration process of cement pastes. The Scientific Bulletin of VALAHIA University – MATERIALS and MECHANICS, nr. 11(14), pp. 23-26, 2016.

The Scientific Bulletin of VALAHIA University
MATERIALS and MECHANICS –Vol. 16, No. 15

DOI 10.1515/bsmm-2018-0012

RESEARCHES REGARDING THE INFLUENCE OF ALLOYING ELEMENTS ON THE MECHANICAL PROPERTIES OF LAMELLAR GRAPHITE CAST IRON

Elena Valentina STOIAN, Vasile BRATU, Cristiana Maria ENESCU, Dan Nicolae UNGUREANU

Valahia University of Targoviste, Faculty of Materials Engineering and Mechanics,
Department of Materials Engineering, Mechatronics and Robotics
13 Aleea Sinaia Steet, Targoviste, Romania

E-mail: cristiana_enescu@yahoo.com

Abstract : *Aim of the study is to present the technological process of obtaining cast iron with lamellar graphite for use in the manufacture of cylinder liners, and to identify the main alloying elements and track their influence on the mechanical properties of cast iron with lamellar graphite.*
Also paper presents analysis of 20 batches of cast iron with lamellar graphite, which are made of cylinder liners, in terms of chemical composition and the mechanical properties.
After the analysis of the 20 castings of cast iron Fc 250 it is observed that: the increase in the carbon content shows a decrease of the tensile strength and hardness of the gray cast iron; the increase in silicon content shows a decrease in hardness and tensile strength. Decreasing the amount of graphite and especially the alloy of silicon iron lead to hardness increase 1% Si increases hardness by 50 HB). A statistical analysis has been performed on the data obtained that accounts for changes in alloying additions. A modeling and optimization of mechanical properties (tensile strength and hardness) was performed according to the percentages of carbon, silicon and manganese. Mathematical modeling found that the hardness and traction resistance of the cast iron decreased with the increase in carbon, silicon and manganese content.

Key words: *Cast iron, mechanical properties, alloying elements*

1. INTRODUCTION

Nowadays, there is a strong demand for cheap materials with mechanical properties able to withstand the requirements of high power automotive engines.
Lamellar graphite cast iron is commonly used in diesel engine applications such as piston rings–cylinder liner where an excellent combination of physical and tribological properties is essential to avoid scuffing and bore polishing issues. The excellent tribological behaviour of lamellar graphite iron alloys is related to the graphite lamellas, which act as solid lubricant agents by feeding onto the tribosurfaces under sliding conditions.

The ratio of ferrite to pearlite in the matrix of lamellar graphite cast irons is known to depend mainly on three parameters like the cooling rate during the eutectoid transformation [1-7], the shape and length of lamellar resulting from the solidification step [8, 9] and alloying elements [1, 2, 6, 10-15].

The mechanical properties of complex multiphase cast iron alloys are largely affected by chemical composition, cooling rate, and technological melt treatments, all of which can cause local variations in the microstructures of the cast parts, and thus differing local mechanical properties. Hence, predicting of microstructure evolution during solidification is a key factor in ensuring desirable mechanical properties and quality of the final casting. This enables the modelling and prediction of the room-temperature microstructure and final mechanical properties of a cast component.

2. PROBLEM SOLUTION– MICROSTRUCTURAL ANALYSIS

For study the influence of composition chemical elements on the mechanical characteristics of lamellar graphite cast iron were analyzed a total of 20 batches.
Of the 20 batches for 2 of these, microscopic analysis was performed.

The mechanical properties of the cast iron depend on the quality of the basic structure and on the size, shape and distribution of the graphite. Since the amount of graphite varies only within relatively small limits, the hardness of the cast iron depends mainly on the composition of the base mass. Iron hardness decreases to increase ferrite content and increases in increasing cementite and phosphorus content [16-19].

A gross or very open network is unfavorable. The base metal is dark colored to black, while the phosphorus

eutectic appears clearly at the grain boundaries as an open-structural structural component [20-25].Cast iron with the best wear-resistance properties is of a high-phosphate-rich, high-phosphate base and thick graphite blades, as shown in figures 1-4.

Figure 1. Microstructural appearance on an unetched sample. Perlite, max. 5% ferrite and lamellar graphite with graphite lamellae length 4 -5 (batch 1) Magnification x100

Figure 2. Microstructural appearance on a sample etched with Nital 5%. Perlite, maximum ferrite 1% and eutectic phosphorus 4-5 (batch 1) Magnification x100

The gray cast iron has the structural component characteristic of the gray lamellar graphite visible on polished samples. After the etching with nital, the nature of the metallic mass is also highlighted. The structure of a perlite-cementitious gray pigment (stains) contains lamellar graphite without secondary cementitious grains.

The gray phosphorous cast iron has in its structure besides the perlite, ferrite and lamellar graphite, the phosphorus eutectic disposed at the limit of the pearlitic grains, schelet-shaped.

Figure 3. Microstructural appearance on an unetched sample. Perlite structure, max. 5% ferrite and lamellar graphite with graphite blade length 4 (batch 2) Magnification x100

Figure 4. Microstructural appearance on a sample etched with Nital 5%. Perlite Structure, Ferrite 1% and Eutectic Phosphorus 5 (batch 2) Magnification x100

The gray cast iron graphite lamellas have a low density, which causes a phenomenon of volume expansion upon solidification (the design of casting molds), which results in a superior quality of the casting surfaces.

3. EXPERIMENTAL PROCEDURES

The raw materials and auxiliary materials required for cast iron production are: cast iron; scrap iron, free of grease, paint and moisture; dry graphite from the arcing of the arc furnace electrodes containing about 90% carbon; 75% ferrosilicon with 5-15 mm grain size and calcined; dry carbide of 2-7 mm granulation; coagulant of slag; ash soda.

Approximately 100-200 kilograms of residual liquid iron after the previous discharge to which we know exactly the chemical composition after the final test and which corresponds to Table 2, is added the calculated graphite for 3.1-3.3% C and the cast iron blocks of the known composition.

Tabel 1. Chemical composition of liquid cast iron

C	Mn	Si	$S_{max.}$	P	Cr	$Cu_{max.}$	$Ni_{max.}$
%							
3.1 - 3.3	0.6 - 0.9	2.4 - 2.8	0.10	0.4 - 0.5	0.4 - 0.6	0.5	0.5

It is filled with iron and cast iron up to 1000 kg. Alloying with ferrophosphorus is done for 0.4-0.5% and for chromium 0.4-0.6%.
Heat the liquid bath and send it to the spectral lab to perform the composite analysis for the alloying elements and not only.
This sample is particularly concerned with the percentage of carbon that must not exceed 3.3% and the percentage of silicon that must be at this stage of 1.7-1.8%.

The percentage of manganese will be in the range of 0.6-0.9% and maximum sulfur 0.10%. Depending on the percentage achieved for sulfur, it is not desulfurization by spilling into the additional pot and reintroducing the liquid into the furnace.

The temperature before the start of desulphurisation should be 1480-1510 ° C and the shotgun. About 300 kg of liquid iron is discharged into a heated pot over 13.5 kg of carbide. Liquid cast iron is shaken for 5 minutes; the carbide slag is discharged from the pot. The furnace will remain in place all the time until the liquid iron is reintroduced. After desulphurisation, a sample will also be taken to determine the chemical composition in particular to visualize the percentage of sulfur. The addition of aluminum will be about 20 grams.

Once the chemical composition is mastered, the metal bath is heated to 1460-1470^{0}C. Under these conditions it can be evacuated and the evacuation is done in a well-heated pot of about 25 kg capacity. When discharging into the pouring furnace, the 75% ferric silicon correction is performed for 2.4-2.9% Si, 100% of the slag is removed.
The feeding of the centrifugal casting machine to obtain cast iron cylinders is done with a special heated spoon and properly protected with film sand.
The final sample must correspond to the composite chemical composition.
After completion of the elaboration and casting, the following chemical compositions and mechanical properties, as shown in Table 2, were obtained.

For study the influence of composition chemical elements on the mechanical characteristics of lamellar graphite cast iron were analyzed a total of 20 batches.

Tabel 2. Chemical compositions and mechanical properties

Batch	C	Si	S	P	Mn	Ni	Cr	Cu	Mg	Pb	HB	R_m [N/mm^2]
1	3.23	2.73	0.029	0.45	0.73	0.2	0.49	0.06	0.01	0.003	248	298
2	3.29	2.35	0.052	0.45	0.7	0.13	0.48	0.11	0.01	0.003	242	284
3	3.22	2.55	0.037	0.45	0.6	0.09	0.46	0.01	0.01	0.003	250	302
4	3.20	2.46	0.037	0.45	0.6	0.09	0.46	0.01	0.01	0.003	255	310
5	3.29	2.8	0.06	0.45	0.75	0.09	0.48	0.06	0.01	0.003	240	283
6	3.28	2.57	0.05	0.45	0.68	0.1	0.47	0.07	0.01	0.003	243	287
7	3.24	2.64	0.036	0.45	0.75	0.17	0.52	0.17	0.01	0.003	246	295
8	3.21	2.49	0.031	0.45	0.73	0.25	0.41	0.25	0.01	0.003	251	307
9	3.27	2.70	0.032	0.44	0.64	0.09	0.47	0.06	0.01	0.003	245	290
10	3.24	2.58	0.024	0.45	0.71	0.14	0.47	0.06	0.01	0.003	247	294
11	3.22	2.55	0.037	0.45	0.6	0.09	0.46	0.01	0.01	0.003	252	304
12	3.27	2.47	0.038	0.44	0.67	0.18	0.49	0.18	0.01	0.003	244	291
13	3.25	2.57	0.068	0.4	0.71	0.18	0.41	0.14	0.01	0.003	243	293
14	3.3	2.67	0.058	0.45	0.7	0.12	0.48	0.1	0.01	0.003	212	220
15	3.3	2.69	0.037	0.44	0.71	0.15	0.48	0.01	0.01	0.003	215	225
16	3.28	2.4	0.04	0.45	0.74	0.16	0.48	0.1	0.01	0.003	224	237
17	3.23	2.42	0.02	0.45	0.77	0.23	0.62	0.21	0.01	0.003	231	242
18	3.21	2.49	0.031	0.45	0.73	0.25	0.41	0.25	0.01	0.003	221	232
19	3.15	2.61	0.03	0.45	0.74	0.14	0.42	0.16	0.01	0.003	225	236
20	3.24	2.44	0.027	0.45	0.79	0.34	0.54	0.28	0.01	0.003	240	262

With data from Table 2, graphical dependencies such as the influence of the carbon, silicon and manganese content on the mechanical properties (Rm, HB).

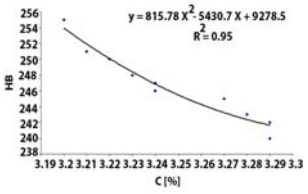

Figure 5. The variation of proportion of carbon with Hardness

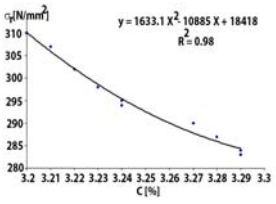

Figure 6. The variation of proportion of carbon with tensile strength

The correlation coefficient is very good, with a value of 0.96, which means that the reproducibility of the experimental data is very good.
Regression equations traced for tensile strength and toughness indicate significant correlation coefficients very close to value 1.
As the carbon content increases, there is a decrease in tensile strength and hardness.

This variation is easily observable in the case of obtaining second degree polynomial correlations. To obtain maximum values for this feature, the optimum range for carbon content is 3.3-3.15%.

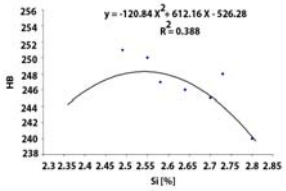

Figure 7. Variation of hardness with percentage of silicon

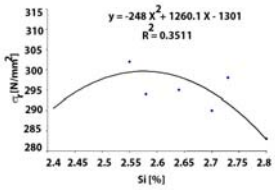

Figure 8. Variation of tensile strength with percentage of silicon

Regarding the analysis of tensile strength and hardness by percentage of silicon, a corresponding correlation coefficient was not obtained.
When increasing the silicon content, there is a decrease in hardness and tensile strength. Decreasing the amount of graphite and especially the alloy of silicon iron lead to hardness increase (1% Si increases hardness by 50 HB).

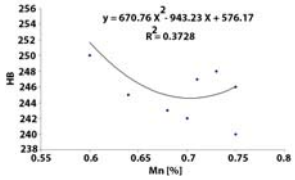

Figure 9. Variation of hardness with percentage of manganese

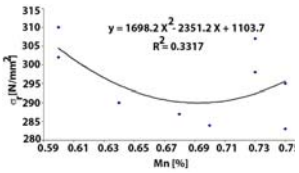

Figure 10. Variation of tensile strength with percentage of manganese

Regarding the analysis of tensile strength and hardness according to the percentage of manganese, a corresponding correlation coefficient was not obtained.
The mechanical properties are influenced by the action of manganese and sulfur on the degree of graphitization, the percentage of perlite in the structure, the amount and type of sulphides.

The increase in manganese content results in an increase in tensile strength, mainly due to its perlitic action. The hardness of the cast iron is increased when increasing the manganese content, the values obtained for hardness being even higher as the degree of saturation in the carbon of the cast iron is lower.

4. MODELING OF MECHANICAL PROPERTIES

For the three factors x_1 (%C), x_2 (%Si) and x_3 (%Mn), it is proposed a mathematical model like this :

$$y = f(x_1, x_2, x_3), \text{ meaning } y = b_0 + b_1x_1 + b_2x_2 + b_3x_3 + b_{12}x_{12} + b_{13}x_{13} + b_{23}x_{23} \quad (1)$$

Table 3. Initial data calculation

Level of variation	Carbon [%]	Silicon [%]	Manganese [%]
Coding variables	x_1	x_2	x_3
Superior level (+)	3.3	2.73	0.79
Lower level	3.225	2.54	0.695
Lower level (-)	3.15	2.35	0.6
Variation gap. Δx_i	0.075	0.19	0.095

To research the mechanical properties of lamellar graphite cast iron studied (R_m [N/mm^2] = Y_1 and HB = Y_2) , according to the proposed model consists of $2^3 = 8$ experience, it used a matrix wich is presented in table 4.

Table 4. Matrix experimentation

No.exp.	Level variables							Lamellar graphite cast iron	
	x_0	x_1	x_2	x_3	x_1x_2	x_1x_3	x_2x_3	Y_1	Y_2
1	+1	+1	+1	+1	+1	+1	+1	298	248
2	+1	-1	+1	+1	-1	-1	+1	284	242
3	+1	+1	-1	+1	-1	+1	-1	310	255
4	+1	-1	-1	+1	+1	-1	-1	283	240
5	+1	+1	+1	-1	+1	-1	-1	307	251
6	+1	-1	+1	-1	-1	+1	-1	290	245
7	+1	+1	-1	-1	-1	-1	+1	242	231
8	+1	-1	-1	-1	+1	+1	+1	232	221

b_i coefficients for each property separately, Y1 and Y2 are determined by equation 2:

$$b_i = \frac{\sum_{u=1}^{N} x_i y_u}{\sum_{u=1}^{N} x_{iu}^2} \quad (2)$$

The calculation to determine the regression coefficients values, values are tabulated in Table 3.

Table 5. The coefficients of the regression

Lamellar graphite cast iron	R_m [N/mm^2]=Y_1	HB=Y_2
b_0	280.75	241.625
b_1	8.5	4.625
b_2	14	4.875
b_3	13	4.625
b_{12}	-0.75	-1.625
b_{13}	1.75	0.625
b_{23}	-16.75	-6.125

$$Y_1 = 280.75 + 8.5x_1 + 14x_2 + 13x_3 - 0.75x_1x_2 + 1.75x_1x_3 - 16.75x_2x_3 \quad (3)$$

$$Y_2 = 241.625 + 4.625x_1 + 4.875x_2 + 4.625x_3 - 1.625x_1x_2 + 0.625x_1x_3 - 6.125x_2x_3 \quad (4)$$

$$x1 = \frac{C - 3.225}{0.075}; x2 = \frac{Si - 2.54}{0.19}; x3 = \frac{Mn - 0.695}{0.095} \quad (5)$$

With the help the test Fischer (F), which is calculated using the equation 6, we had verified if the regression equations obtained previously are good.

$$F_{calcul} = \frac{s_1^2}{s_r^2} = \frac{miscalculation}{error\ experimentation} \quad (6)$$

$$s_1^2 = \frac{\sum_{i=1}^{n} (y_{exp} - y_{calc})^2}{n - k - 1} \quad (7)$$

$$s_r^2 = \frac{\sum_{i=1}^{n} (y_{exp\,1} - y_{exp\,2})^2}{n - 1} \quad (8)$$

where: y_{ex} - experimentation results;

y_{calc} - the results of the calculation;

y_{ex1} - Y variation value experience 1;

y_{ex2} - Y variation value experience 2;

n - number of experiences (8 experiences);

k - three factors studied.

According to Fischer test [26, 27], equations mathematical model (equations obtained 3, 4 ,5) are correct if $F_{calcul} < F_{tabel\ (\alpha,k,n)}$ equations proposed model are incorrect or if $F_{calcul} > F_{tabel\ (\alpha,k,n)}$ (ie not correspond equations 3, 4, 5).

Using the test equation Y2 (4), which gives depeneding hardness per unit of carbon content, silicon and manganese, we tried to tested the Fisher.

$$Y_2 = 241.625 + 4.625x_1 + 4.875x_2 + 4.625x_3 - 1.625x_1x_2 + 0.625x_1x_3 - 6.125x_2x_3 \quad (9)$$

The results are presented in Table 6.

Table 6. Experimental and calculated values of hardness per unit

Exp. No.	$Y_{2\ exp.}$	$Y_{2\ calc.}$	$Y_{2\ exp.} - Y_{2\ calc.}$
1	248	248.625	-0,625
2	242	241.75	0.625
3	255	254.375	0.625
4	240	240.875	-0.875
5	251	251.625	-0.625
6	245	245.625	-0.625
7	231	231.625	-0.625
8	221	220.375	0.625

Using the relationship 7, and knowing that n = 8, k= 3 is calculated

$$s_1^2 = \frac{\sum_{i=1}^{n}(y_{exp} - y_{calc})^2}{n-k-1} = \frac{7.56}{4} = 1.89$$

Repeating experience the same conditions are obtained these data.

Table 7. Percentage hardness values in two experiences

Exp. No.	$Y_{2exp.1}$	$Y_{2exp.2}$	$Y_{2exp.1} - Y_{2exp.2}$
1	248	248.625	*-0.625*
2	242	239.375	*2.625*
3	255	238.875	*16.125*
4	240	229.625	*10.375*
5	251	239.375	*11.625*
6	245	230.125	*14.875*
7	231	229.625	*1.375*
8	*221*	*220.375*	*0.625*

Using relationship number 8, we get

$$s_r^2 = \frac{\sum_{i=1}^{n}(y_{exp\ 1} - y_{exp\ 2})^2}{n-1} = \frac{733\ .625}{7} = 104\ .8035$$

From the relation 6, we get:

$$F_{calcul} = \frac{s_1^2}{s_r^2} = \frac{1.89}{104\ .8035} = 0.018$$

According anexes [27], for α=0.05, h(υ_1)=3, n(υ_2)=8, we'll have a F=4.07.
Since $F_{calcul} < F_{tabel\ (\alpha,k,n)}$, meaning 0.018 < 4.07, it follows that the proposed mathematical model is correct and also the equation:

$$Y_2 = 241.625 + 4.625x_1 + 4.875x_2 + 4.625x_3 - 1.625x_1x_2 + 0.625x_1x_3 - 6.125x_2x_3 \quad (10)$$

correctly describes the correlation between hardness per unit and quantities of carbon, silicon and manganese.

5. CONCLUSIONS

From equations 3, 4 and 5 we conclude that hardness and traction resistance decrease with increasing carbon, silicon and manganese content (coefficients b1 and b2 are positive).

Carbon and silicon are the most important grafitizing elements, their variation causing the greatest changes in the cast iron structure studied. Carbon is found in cast iron either in free (graphite) or bonded (cementite), and silicon is mostly dissolved in ferrite.

Influence of manganese is relatively low. Increasing manganese content leads in the first part to the reduction of bound carbon, so in this case the manganese exhibits a grafitizing action. The further increase in manganese content is manifested by its anti-graphitizing action.

Increasing the manganese content results in an increase in traction resistance.

The hardness of the cast iron is also increased when increasing the manganese content, the values obtained for hardness being higher as the degree of carbon saturation of the cast iron is lower.

Statically point of view analisyed the ecuation Y_1 and Y_2 were found "in accordance" on the basis of the Fischer criterion wich means that the model is good and suports the reproductibility of the trial experiments.

In this case the answer variables Y1, Y2 (representing the equation of the mathematical model proposed) has been corelated with x_1, x_2, x_3 (representing the variation of percentages of carbon, silicon and manganese according to table 2 and with relations 3,4,5).

From the analyzes carried out it was found that for a high tensile strength the structure of the metallic shell of the cylinders must be perlite.

Pearl-cast iron has high tensile strength but low elongation.

The percentage of ferrite decreases with the increase in the percentage of manganese, because manganese is a perlite element, favoring the appearance of carbides in the structure.

When increasing the silicon content, there is a decrease in hardness and tensile strength. Decreasing the amount of graphite and especially the alloy of silicon iron lead to hardness increase (1% Si increases hardness by 50 HB).

As the carbon content increases, there is a decrease in tensile strength and hardness.

Increasing manganese content leads in the first part to the reduction of bound carbon, so in this case the manganese exhibits a grafitizing action. The further increase in manganese content is manifested by its anti-graphitizing action.

The increase in manganese content results in an increase in tensile strength, mainly due to its perlitic action. The hardness of the cast iron is increased when increasing the manganese content, the values obtained for hardness being even higher as the degree of saturation in the carbon of the cast iron is lower.

REFERENCES:

[1] B.V. Kovacs: AFS Trans. Vol. 89 (1981), p. 79-96.

[2] E.N. Pan, M.S. Lou and C.R. Loper: AFS Trans. Vol. 95 (1987), p. 819-840.

[3] L. Guerin and M. Gagne: The Foundryman Vol. 80 (1987), p. 336-344.

[4] G.M. Goodrich and R.W. Lobenhofer: AFS Trans., (2007).

[5] C. O. Rusănescu M. Rusănescu, F. V. Anghelina, V. Bratu, The influence of the micro-alloying elements on physical and structural characteristics of the some steel destined for manufacturing the oil pipes, Romanian Reports in Physics, Vol. 68 (1), (2016), p 278–293.

[6] C.O.Rusanescu, M. Rusanescu, The stress-strain curves determined for microalloy steel with v determined on the torsion tests, Metalurgia (Bucharest) 59.(1) (2007):p 38-44.

[7] J. Sertucha, P. Larranaga, J. Lacaze and M. Insausti: Int. J. Metalcasting Vol. 4 (2010), p 51-58.

[8] J. Sertucha, R. Suarez, J. Izaga, L.A. Hurtado and J. Legazpi: IJCMR Vol. 16 (2006), p. 315-322.

[9] H. Takeda, K. Asano and H. Yoneda: Int. J. Cast Met. Res. Vol. 21 (2008), p. 81-85.

[10] C.O.Rusanescu, M. Rusanescu, The stress-strain curves determined for microalloy steel with v determined on the torsion tests, Metalurgia (Bucharest) 59.(1) (2007): 38-44.

[11] Rusanescu C. O., Jinescu C., Paraschiv G., Biris S. St., Rusanescu M., Ghermec O., Influence of the Nb, V and Mo Elements on the Ecological Micro-alloyed Steel Properties, Revista de chimie, Volume: 66, Issue: 5, (2015), p: 754-757.

[12] T. Levin, P.C. Rosenthal, C.R. Loper and R.W. Heine: AFS Trans Vol. 79 (1971) p.493-514.

[13] T. Kanno, T. Kikuchi, I. Kang and H. Nakae: AFS Trans., (2005).

[14] G.S. Cho, K.H. Choe, K.W. Lee and A. Ikenaga: J. Mater. Sci. Tech. Vol. 23 (2007), p. 97-101.

[15] G.H. Hsu, M.L. Chen and C.J. Hu: Mater. Sci. Eng. A, Vol. A444 (2007), p. 339-346.

[16] I. Riposan, M. Chisamera and S. Stan: Int. J. Cast Met. Res. Vol. 20 (2007), p. 64-67.

[17] T. Nobuki, M. Hatate and T. Shiota: Int. J. Cast Met. Res. Vol. 21 (2008), p. 31-38.

[18] Petre, Wear model of sliding surfaces used in the machine-tools industry, The Scientific Bulletin of Valahia University, Materials and Mechanics, nr.9 (year 12) (2014),p. 99-104.

[19] Sofroni, L., Ștefănescu, D.M. și Vincenz, C. Fonta cu grafit nodular. Editura Tehnică, București. 1987.

[20] Ivona Camelia Petre, Ileana Nicoleta Popescu, The phenomenological analysis of the nature of the friction, from theoretical and experimental point of view of Al-Al_2O_3-graphite composite /cast iron „pin on disc" sliding system, International Journal of Mechatronics and Applied Mechanics, (2017), Issue 2.

[21] Sofroni, L., Ripoșan, I., Brabie, V. și Chișamera, M. Turnarea fontei. Editura Didactică și Pedagogică, București. 1985.

[22] A. Josan, D. Petre, I. Kiss.: Studies and researches on the influence of chemical composition of cast rolls made of hypereutectic steel, on their hardness in exploatation, Scientific Conference Research and Development of Mechanical Elements and Systems Jahorina – IRMES, Sarajevo, Bosnia & Hertegovina, 2002.

[23] Joan Serrallach, Jacques Lacaze, Jon Sertucha, Ramón Suárez, Adrián Monzón, Effect of Selected Alloying Elements on Mechanical Properties of Pearlitic Nodular Cast Irons, Key Engineering Materials Vol. 457 (2011) p. 361-366.

[24] C. O. Rusănescu M. Rusănescu, F. V. Anghelina ,T. Iordanescu, Mathematical relation ships between alloying elements and technological deformability indexes, Journal of Optoelectronics and Advanced Materials 15(7) (2013), p.718-723.

[25] Rusanescu C. O., Jinescu C., Rusanescu M., Enescu M. C., Anghelina F. V., Stoian E. V., Despa V., Mathematical Modelling of the Stress-Strain Curve for 31VMn12 Ecological Steel, Materiale plastice, Volume: 54, Issue: 3, (2017), p. 409-413.

[26]D.Taloi, E. Florian, C.Bratu, E.Berceanu, The optimization of metallurgical processes, Bucharest 1983.

[27]I.Ciuca, S.Dimitriu, Modelarea si optimizarea proceselor metalurgice de deformare plastic si tratamente termice, Editura Didactica si Pedagogica, Bucharest, 1998.

The Scientific Bulletin of VALAHIA University
MATERIALS and MECHANICS –Vol. 16, No. 15

DOI 10.1515/bsmm-2018-0013

TRIBOMETRIC DEVICE FOR DETERMINING FRICTION FORCES AND FRICTION COEFFICIENTS IN THE CASE OF DRY FRICTION OF MATERIALS

Ivona Camelia PETRE, Adrian CATANGIU, Ileana Nicoleta POPESCU, Dan Nicolae UNGUREANU, Alexis Daniel NEGREA, Aurora Anca POINESCU, Maria Cristiana ENESCU, Elena Valentin STOIAN, Veronica DESPA

Valahia University of Targoviste, Faculty of Materials Engineering and Mechanics,
13 Aleea Sinaia Street,Targoviste, Romania

E-mail: acatangiu@yahoo.co.uk

Abstract: *The aim of the paper was to develop a device ("pin-on-disc" type) for the measurement of friction in plane friction couplings with sliding movement. On tribometric device (made in our laboratory) we can measure the friction force, friction coefficient and wear, for different loading conditions, speeds, time and material coupling.*

For the measurement of the frictional force as well as of the coefficients of friction, mainly the method with a resistive tensiometric transducer is used. With a DataQ DI 245 data acquisition board it is possible to record up to 2 kHz frequencies in the range of -10 ÷ +10 mV with a resolution of 13 bits. To test the functionality of the device, a preliminary test was carried out for a steel pin- on- cast iron disc, for different values of the normal pushing force. The device was calibrated and the measurement results were recorded and processed on the computer.

Keywords: *Design and manufacturing of tribometric device, Preliminary tests, Friction coeficients, Dry sliding, Steel and cast iron materials.*

1. INTRODUCTION

Experimental research on the evolution of the friction coefficient over time and implicitly with the slip or tread distance allows observing and analyzing the behavior of friction and wear behavior of different material couplers [1-7].

The evolution of the friction coefficient is dependent on the specificity of the tested materials [2-7], the environmental conditions and the kinematic particularities of the test bench. Consideration of the approximately constant friction force at the same normal force, velocity, material, etc., is due to the fact that the number of interactions that occur at a given moment is higher and that the law of statistical distribution of contact processes is approximately constant.

By experimental observations carried out over time, two basic "laws" of friction originated by Amonton in 1699 [8] were deduced:

1) Friction is independent of the apparent contact area of the two bodies.

2) The frictional force is proportional to the normal load between the bodies.

Coulomb in 1785 proposed the "third" law:
3) Friction is independent of sliding speed

The coefficient of proportionality in the second law, $F=\mu \cdot F_n$, is the coefficient of friction. As friction can be static or kinetic, static friction coefficient (μ_s) or kinetic friction coefficient (μ_k) results.

In the literature on explanation of Amonton's laws [9, 10, 11] the following hypotheses are proposed:

1. During sliding, the resistive force on the contact area unit is constant:

$$F_f = A_r \cdot S \tag{1}$$

where: F_f is the frictional force, - A_r the actual contact area, S - the specific friction force (force per unit area).

2. The real contact area, is proportional to normal force F_n:

$$A_r = k \cdot F_n \tag{2}$$

where k is a constant of proportionality.
By eliminating A_r, it follows:

$$F_f = S \cdot k \cdot F_n \tag{3}$$

The first hypothesis is easy to justify, no assumption is made as to the nature of the specific frictional force.

The second hypothesis can not be justified in all cases, but for certain contact conditions, the validity is ensured:

a) For total plastic contact, the actual area does not depend on the topography of the surface;

b) The actual contact area does not depend on how the asperity deforms.

Regarding the third friction law, further research has shown that the frictional force and, implicitly, the coefficient of friction varies within certain limits depending on the sliding speed.

In the case of dry friction, the variation of friction force and coefficient of friction by sliding speed could not be mathematically related due to the complexity of the phenomenon. Thus, for different material couples, it is necessary to experimentally determine the variation of forces and friction coefficients.

The paper aims at design and manufacturing of a tribometric device for the experimental determination of friction forces and friction coefficients for different friction couplings in the case of dry friction under certain load and speed conditions.

Dry sliding involves the absence of lubricant between the contact surfaces in relative motion. At the microgeometry level, the direct contact of the friction surfaces is achieved by surface irregularities or their asperity peaks, and the generation of frictional force takes place at the interfacial contact level due to the elastoplastic deformations between the peaks of the asperities in contact.

II. DESCRIPTION OF THE TRIBOMETRIC DEVICE

2.1 Tribometric device construction (components)

For the measurement of the frictional force as well as of the coefficients of friction, mainly the method with a resistive tensiometric transducer is used. This method is based on the fact that the frictional force produces the displacement or tendency to move one of the parts of the friction coupler, which can be taken over by a resistive tensiometric transducer, the resistance variation being measurable.

The tribometric device (Fig. 1) consists of the following main elements:

- a two-element friction coupler, a disc (2) mounted on the rotatable main wheel (3) and the cylindrical movable test piece (1) mounted in the fixing device (7);
- the main disc (3) is mounted on the main shaft (5) which is caught with radial bearings, fixed to the bearing body (4);
- the main shaft (5) receives the rotation movement from a driving electric motor (8) by means of a flexible (elastic) coupling (6);
- the clamping device (7) of the mobile specimen (1) is rigidly fixed to the fastening columns (10);
- the main shaft or disc spindle speed can be varied by means of a frequency converter;
- loading the fixed cylindrical specimen (1) with the normal load is done by applying weights (13) of different values to the body of the fixing device (7);
- the fixed specimen (1) can be moved to the rotating disc (2) at different diameters (8 ... 16 mm);
- the device is connected to a data acquisition board (12).

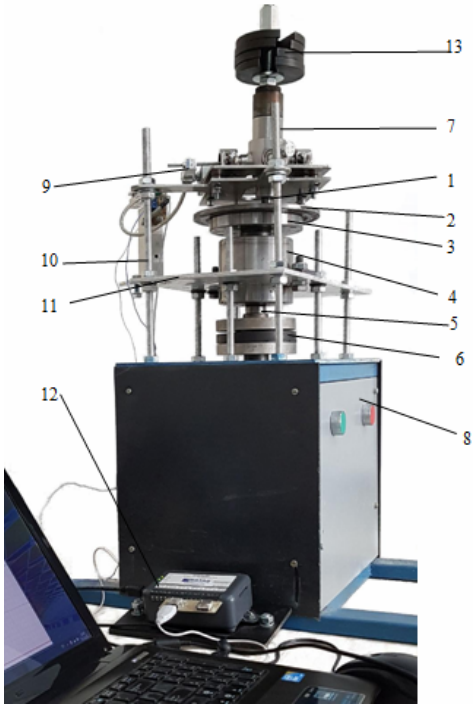

Figure 1. Tribometric device

2.2. Tribometric device characterisitcs

On the designed and manufactured device can be done the following works:

1. Experimental determination of frictional forces and friction coefficients for different friction couplings in the case of dry sliding friction.

2. Experimental determination of the variation of frictional forces and friction coefficients according to the relative sliding velocity for different material couples.

3. Determination of variation of friction coefficients depending on load of different material couples.

4. Comparison of the friction coefficient variation in non-lubricated (dry) lubrication conditions with the one obtained under boundary and mixed lubrication conditions for different couples of materials.

5. Determination of the linear and gravimetric wear intensity for different couples of materials under dry and limiting friction.

6. The deformation and wear of the disc made of a less hard material in contact with the movable specimen in the form of a conical penetrator (of different angles).

III. TEST DEVICE FUNCTIONALITY

For the friction coefficient to be measured in reproducibility conditions, it is necessary to keep constant the relative speed of movement of the elements in contact.
Thus, if the force of normal pressure and frictional force are known, the product of relation (3) can be determined.
The normal force is controlled by applying to the pin support element some metal discs with known mass.

The friction force is measured with a force transducer shaped like a parallelepiped beam whose bending is taken over by resistive tensiometric sensors mounted in the Wheatstone deck.

The maximum load capacity of the transducer is 100N and the signal supplied by the transducer (sensitivity) according to the manufacturer's specifications is approximately 1mV / V at the maximum load limit. For a 5V supply voltage, the output signal varies from 0 to 5 mV.

It can be easily monitored with a DataQ DI 245 data acquisition board that allows up to 2kHz frequencies to be recorded in the -10 ÷ +10 mV range with a resolution of 13 bits.

The transducer was made on the stand, outside the machine, using calibrated masses. Figure 2 shows the static characteristic of the friction force transducer.

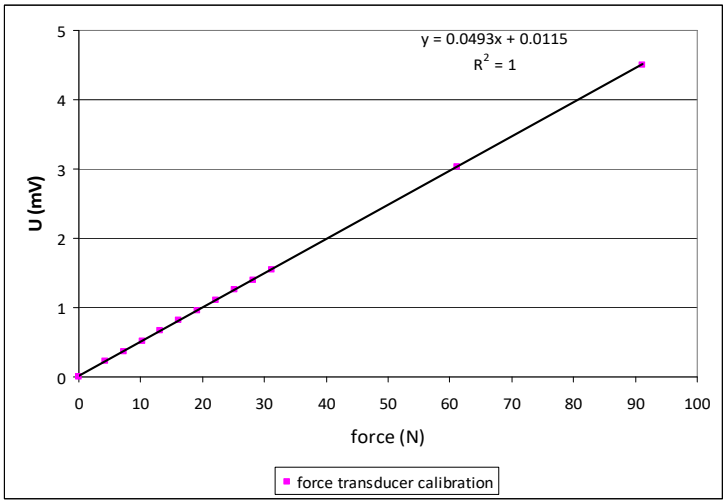

Figure 2. The static characteristic of the friction force transducer

At the data acquisition, it is possible to generate an "event handler" by simply pressing a button on the acquisition board that can be used as a marker for the test parameter variation times.

Thus, in order to estimate the ratio F_f/F_n for a larger number of normal pressures, during the recording of the frictional force values the normal pressing force can be changed and the event marker can be read in order to know, at the later analysis, the moment of occurrence of the it. Such an estimate is based on the assumption that during the experiment, the friction conditions remain approximately constant (no contact wear occurs).

To test the functionality of the device, a preliminary test was carried out for a steel pin- on- cast iron disc for five normal pushing force values. Figure 3 illustrates the dependence between the normal push force and the frictional force monitored during the test.

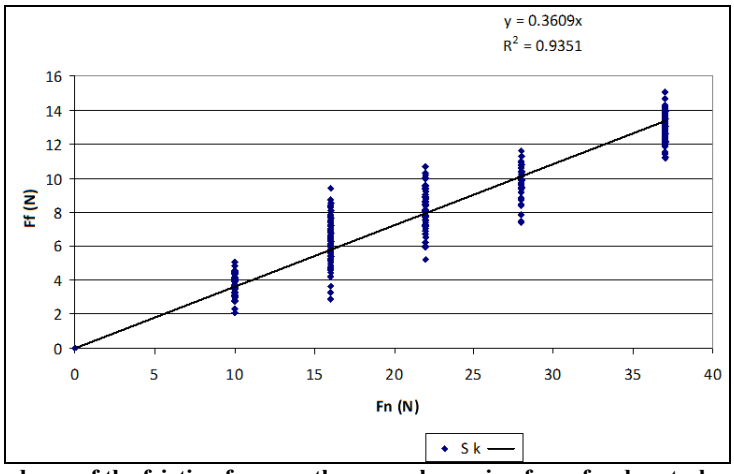

Figure 3. Dependence of the friction force on the normal pressing force for dry steel-cast iron friction

The variability of the friction force recorded by the transducer for the same value of the normal push force is due to the surface quality of the disc, its roughness contributing to the application of the normal push force in dynamic mode.

This is obvious because the friction is influenced by the contact between the peaks of asperities that escalate over the others in the sliding between surfaces.

IV. CONCLUSIONS

The realization of the tribometric device is intended to be an instrument in support of the formation of concepts regarding the phenomena related to friction, wear and lubrication of the friction couplers.

The points highlighted in the proposed experimental work can be considered as a starting point for choosing the material of a friction coupler, the mode of lubrication, and why not, the mode of operation of the friction coupler.

Based on the experimental results obtained, optimal construction solutions can be found from the point of view of the phenomena related to friction, wear and lubrication of the friction couplings.

In the future, there are several improvement perspectives of the tribometric device.

For the investigation of the wear (variation of friction coefficient with the mutual slipping distance of the elements in contact), it is necessary to estimate this distance easily and the next step in the development of the device will be speed monitoring with the acquisition plate using a rotation counting element of the type of the photo ensemble -diodă-photo-transistor.

Also, is tested the possibility of replacing the application mode of the normal push force with a system that including a force transducer and allows, in addition, to monitoring and variation of its, without stopping the device.

REFERENCES:

[1] Tudor A, Vlase M. – Uzarea materialelor, Ed. Bren Bucureşti (Bren Press, Bucharest), 2010.

[2] Petre, I.C., Popescu, I.N., The Phenomenological Analysis Of The Nature Of The Friction, From Theoretical And Experimental Point Of View Of Al-Al2O3-Graphite Composite/Cast Iron „Pin On Disc" Sliding System. International Journal of Mechatronics and Applied Mechanics, 2017 (2), pp.40-47.

[3] Popescu, I.N., Petre, I.C., Despa, V., Analytical and Experimental Studies on Wear Behaviour of Cast and Heat Treated AlSi 12 CuMgNi and AlZn 6 MgCu Matrix Composites Reinforced with Ceramic Particles, Under Sliding Conditions. Proceedings of the International Conference of Mechatronics and Cyber-MixMechatronics, Springer International Publishing , 2018, pp. 71-82.

[4] Popescu, I. N., Zamfir, S., Anghelina, V. F., & Rusanescu, C. O. (2010). Processing by P/M route and characterization of new ecological Aluminum Matrix Composites (AMC). *International Journal of Mechanics*, *4*(3), pp. 43-52.

[5] Rusanescu, C.O., Rusanescu, M., Jinescu, C., & Biris, S.S. (2018). Laser Hardening Influence of Metal Surfaces. *Materiale Plastice*, *55* (2), pp. 184-187

[6] Rusanescu, C.O., Rusanescu, M., Anghelina, F.V., & Popescu, I.N. (2018). Study Deformability Ecological Steel (41Cr4). *Materiale Plastice*, *55*(3), pp. 357-360.

[7] Petre, I., & Tudor, A. (2003). Friction and wear model for polymer and cast iron couple, The Annals of University "Dunărea De Jos" of Galaţi Fascicle VIII, Tribology 2003, pp. 107-111.

[8] Bowden, F. P., and Tabor, D., "The Friction and Lubrication of Solids", Oxford University Press, New York, p. 1950.

[9] Arnell, R.D., Davies, P.B., Halling, J., Whomes, T.L., Tribology- Principles and design applications**,** Mac. Millan, 1991.

[10] Pavelescu, D., Musat, M., Tudor, A., Tribologie, Ed. Did. si Pedagogica Bucuresti, 1977.

[11] Rabinowicz, E., Friction and wear of materials, New York, John Willy Inc., 1985.

The Scientific Bulletin of VALAHIA University
MATERIALS and MECHANICS –Vol. 16, No. 15

DOI 10.1515/bsmm-2018-0014

STRUCTURAL ASPECTS REVEALED BY SEM INVESTIGATIONS FOR 2024 ALUMINUM ALLOYS

Florina Violeta ANGHELINA, Dan Nicolae UNGUREANU, Carmen POPA, Elena Valentina STOIAN, Ileana Nicoleta POPESCU, Cristiana Maria ENESCU, Constantin C. ANGHELINA

Valahia University of Targoviste, Faculty of Materials Engineering and Mechanics,
Department of Materials Engineering, Mechatronics and Robotics,
13 Aleea Sinaia Street, Targoviste, Romania

E-mail: vianghelina@yahoo.com

Abstract. *In this presentation are evidenced instrumental characterization by Electronic Scanning Microscopy (SEM) equipped with EDS / WDS of aluminum alloys such 2024 alloy with multiple synergistic purposes as: acquisition of new knowledge, increase the amount of information obtainable about the material, increasing the efficiency and the quality of the tests, characterization of special destination alloys and assessing their conformity with the specified requirements. In this direction, it requires both the knowledge the test methods (theoretical basis, test method, procedure relating to the method, quality assurance testing) as well material characteristics investigated. These aspects are necessary for test system design, and preliminary interpretation of experimental results.*

Keywords: *The 2024 aluminum alloys, conformity assessment alloys, electron microscopy.*

1. INTRODUCTION

In brief, the information needed to interpret the results obtained will be briefly presented.

These are: the general characteristics of aluminum alloys and those of type 2024 alloys, the method and working technique used, the results obtained and their corroborated analysis[1-3].

The analysis of the results will be done in terms of the quality of the test, and less in terms of satisfying the usage requirements, because the decision to use the alloy belongs to the engineers and material science specialists.

In industrial applications, aluminum is not used in pure state because it has inadequate mechanical and physico-chemical properties, but in the form of alloys, because by alloying it improves its properties. Thus, in order to increase the breaking strength, the flow limit and the hardness, aluminum is alloyed with different elements (Cu, Si, Mg and rarely Mn, Ni, Fe, Cr, Zn).

Aligning always leads to a decrease in the electrical conductivity of the alloy relative to pure aluminum and ductility. In practice, taking into account the aim pursued, a compromise is allowed between the excluded properties and the property of most interest[4-7].

Require characteristics of 2024 aluminum alloys:

- composition required,
- workpiece geometry, etc.

also their inherent characteristics:

- compositional variation,
- grain size,
- nature size,
- and distribution of specific compounds of the alloy matrix or of the non-specific compounds.
- impurity content, etc.

The studied sample is taken from a 2024 aluminum batch produced at S.C. ALRO Slatina. If it is considered that the alloy composition is sufficient to be studied for the proper behavior of the alloy, then other aspects should also be taken into account: microstructure (granulation), content inclusions, compounds that affect mechanical strength, corrosion resistance and wear resistance.

a) 650X

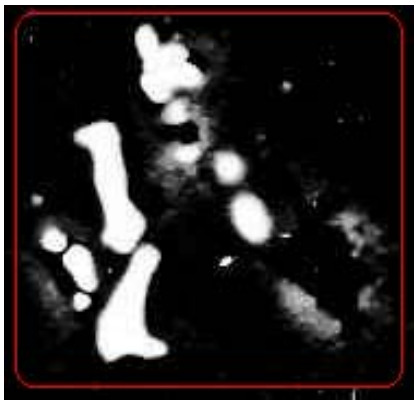

b) part of an enlarged detail of the sample

Figure 1. SEM microscopy image of morphology and element distribution in sample DA-4161

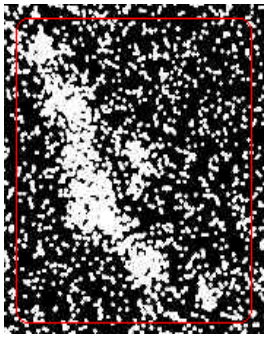

a) part of an enlarged detail of the sample

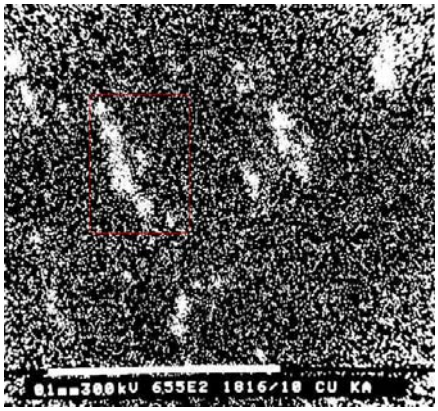

b) 650x

Figure 2. Copper element distribution image of the sample DA-4161

2. EXPERIMENTAL TECHNIQUE

Table 1. Concentration of aluminum alloy elements of duralumin type required by the standard SR EN 573 3: 1994

Elements [%]	Cu	Mg	Zn	Mn	Si	Fe
Composition	3.8-4.9	1.2-1.8	max 0.25	0.3-0.9	max 0.5	max 0.5

The chemical composition of duralumin samples should comply with the requirements of SR EN 573 3: 1994, which specifies the compositional limits of aluminum alloys 2024 (Table 1). From the many heat-curable alloys, the most important are duralumin, which are part of the manganese-added Al-Cu-Mg alloy system (possibly other elements such as Zr, Li, Cr, Be, Ti, Cd , Ag, V).

Conventionally, duralumins are divided into three groups, depending on the contents of the main alloying elements. The sample (charge) studied has the code DA-4161.

The samples were analyzed on a microstructural scale using a SEM BS-350 TESLA electronic microscope equipped with an EDAX device to perform both the composite analysis of the sample and its morphological investigation.

Were collected the samples which have the following codes: DA-4161 batch; type of material: 2024 duralumin

for aviation (AU4G1); treatment: T4 (specified by manufacturer).

3. EXPERIMENTAL RESULTS

SEM-EDAX electron microscopy investigations were performed as specified. The image of figure 1 (at a magnification of 650 times) show the area where the compounds are highlighted by gray shades and their shape. Thus, ellipsoidal compounds or black rounds are the Mg_2Si hardener. This compound appears isolated in the vicinity of the S (Al_2CuMg) phase that has a specific appearance.

In some areas this compound agglomerates into S phase zones. The SEM images are highlighted by gray, but also by their specific shape, compounds incorporated into the DA-4161 batch alloy matrix. S and S 'phases are black and have irregular polygonal morphology. They occupy a significant area of the areas shown in figure 1.

Compounds of the type Al-Cu-Fe are white and have a form of rods or circular morphology. Such images emphasize the presence comparable, in terms of occupied areas in the image, compounds containing Fe, with the S phase (S '). Round shaped strengthener compound Mg_2Si and "color" gray-black is dispersed relatively homogeneous in the sample.

Gray tone of this compound is about the same as the S phase (S '). The distribution of different elements were performed on two microstructures, in a complementary manner so as to cover the major alloying elements beach.

The following figures: figure 2, figure 3, figure 4 and figure 5 are presented the "maps" concentration of the main alloying elements.

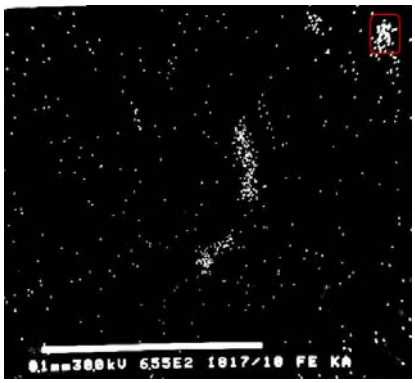

a) 650x

b) part of an enlarged detail of the sample

Figure 3. Iron distribution image in the sample DA-4161

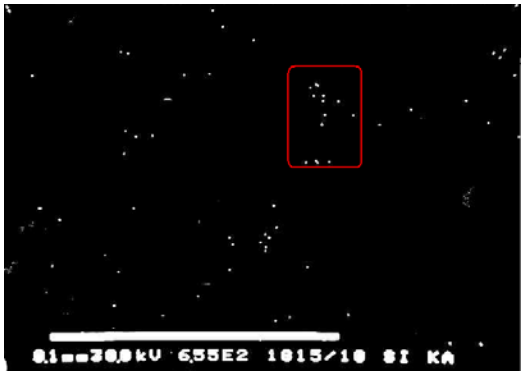

a) 650x

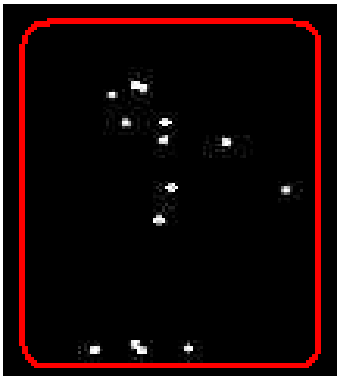

b) part of an enlarged detail of the sample

Figure 4. Silicon distribution image in the sample DA-4161

Inhomogeneous distribution of Copper is revealed by its distribution the previous figures that highlight even higher concentration gradient in the vicinity of clusters of compounds. In terms of the distribution of the compounds most likely drains Fe compounds "color" white (Al7Cu2Fe). A comparative analysis of the distribution of Cu and Fe relative to COMPO image shows that Fe segregates at the interface of matrix-compound. It can be estimated that the Fe concentration gradient interface areas matrix - compounds is higher than that of Cu.

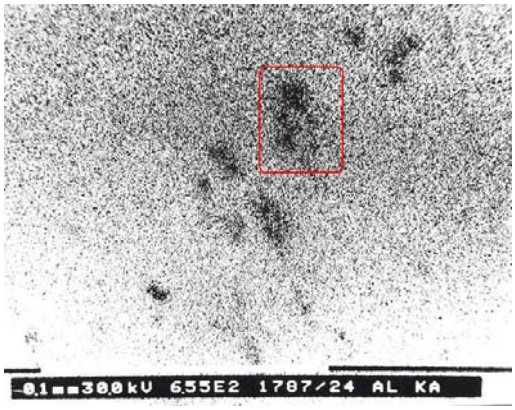

a) 650x

b) central part of an enlarged detail of the sample

Figure 5. Aluminum distribution image in the sample DA-4161

Silicon is very little free areas highlighted both compounds, and the compounds. Basically silicon can be identified in the previous figure, most likely in Mg_2Si compounds. The appearance of relative heterogeneity is revealed than previous figures showing the distribution Aluminium marked border area and shows that, technically there is a heterogeneity of Aluminium concentration distribution at the micrometer scale. Also, the image shows the concentration gradient of aluminum, which has a exponeţial profile from the center of Mg_2Si compounds, by phases S and S ' to the the matrix.

4. CONCLUSIONS

Analyzing the experimental results we can predict the following: Certainly the major phases for the studied sample were identified: Mg_2Si, Al_2CuMg (phases S and S '), Al_7Cu_2Fe.

Iron compounds have a comparable weight to phase S (S '), which can be explained by the zonal segregation of Fe. This is justified by the solubility of Fe in Al. The Al, Cu, Mg elements are distributed relatively homogeneously in the matrix and exhibit segregation compounds.

The Fe and Si compounds are homogeneously distributed and have major characteristics. The aluminum alloy of the type 2024 studied corresponds to the content of the compounds with the class aluminum alloy (4.4% Cu, 1.5% Mg, 0.5 Mn), in which compounds type Mg-Si, Al-Cu-Mg, Al-Cu and Al-Cu-Fe-Mg.

For this batch, iron compounds were not identified by the X-ray diffraction method, but were evidenced by SEM-EDAX analysis. This can be explained by a low level of structural factor and / or structural distortions.

REFERENCES

[1] Sadki, M.L.Hattali, M. A. Bradai, R. Youne, N. Mesrati, Characterization and Modeling of the Mechanical Behavior of Aeronautical Alloy Based Composite, Universal Journal of Chemistry 4(1) (2016) 10-19.

[2] P. Rambabu,N Eswara Prasad et all, Aluminium Alloy for Aerospace Application in: Prasad N.E. and Wanhill R.J.H.(Eds.), Aerospace Materials and Material Technologies, Springer Science, Singapore, 2017, pp 29-52.

[3] encea, Bazele incercarilor spectrochimice de emisie optica prin scanteie si arc electric, Ed. Printech, Bucuresti, 2007.

[4] C.I. Crimu, B. Istrate; C. Munteanu, I. Antoniac, M.N. Matei, K. Earar, XRD and Microstructural analyses on biodegradable Mg alloys, Key Engineering Materials, 638, (2015) 79-84.

[5] J.S. Robinson, W. Redington,The influence of alloy composition on residual stresses in heat treated aluminium alloys, Materials Characterization 105 (2015) 47–55.

[6] I.N. Popescu, D. Bojin, I. Carceanu, G. Novac, F.V. Anghelina, Morphological and structural aspects using electronic microscopy and image analysis of iron powders obtained by water atomization process, Journal of Science and Arts 12, Year 10, No. 1(12), pp. 125-134, 2010.

[7] Carmen Otilia Rusanescu, Marin Rusanescu, The stress-strain curves determined for microalloy steel with determined on the torsion tests, Metalurgia , 59 (1) (2007), 38-44.

The Scientific Bulletin of VALAHIA University
MATERIALS and MECHANICS –Vol. 16, No. 15

DOI 10.1515/bsmm-2018-0015

INTELLIGENT PLATFORM WITH BLDC DRIVES AND MICROSYSTEMS FOR MECHATRONIC APPLICATIONS IN SECURITY AND SURVEILLANCE

Dorin ANGELESCU [1,2], Gheorghe Ion GHEORGHE [1,2]

[1] University of Valahia Târgoviște - Doctoral School of Mechanical Engineering and Mechatronics at Valahia Târgoviște University, Romania

[2] National Institute of Research and Development in Mechatronics and Measurement Technique (INCDMTM), 6-8 Sos. Pantelimon, Bucharest

E-mail: dorinnirod@yahoo.com; geocefin@yahoo.com

Abstract. *Result of the Scientific Concerns from the Doctoral School of Mechanical Engineering and Mechatronics of the Valahia Târgoviște University and the research project of INCDMTM "INTEGRATED MECHATRONIC SYSTEM FOR HUMAN SECURITY INSURANCE FOR THE SAFETY OF OBJECTIVES AND INTERVENTIONS IN RISK - MISO ZONES" (project ID: PED-2016-0924, code PN-III-P2-2.1-PED-2016-0707) in the field of robotics, the scientific work "Intelligent Platform with BLDC Drives and Microsystems for Mechatronic Applications in Security and Surveillance " is the completion of the experimental testing of controlling the movement of a security and surveillance robot, as part of the Ph.D. industrial thesis "Studies, research and contributions on the development of a smart mecatronic robot for security and surveillance applications". The scientific work ultimately results in an intelligent, original platform that will be used to control the movement of the robot. The platform allows communication between the latest generation BLDC engine (embedded in the drive wheel) and it's controller and a computerized microsystem that will handle the displacement controls and will also provide the link with the human operator through any remote guidance system that is used. Although designed for an intelligent security and surveillance mechatronic robot, this platform is proven to be extensively versatile for any other type of robot or mobile platform that uses BLDC wheel-drive engines. The project harmoniously combines Mechatronics, Cyber-MixMeatronic, Integronics and Artificial Intelligence into an Intelligent Interoperable Construction.*

Keywords: *Intelligent platform, Artificial intelligence, Intelligent electric motors control, Intelligent measuring technology.*

1. INTRODUCTION - BLDC ENGINES IN MECHATRONICS

The emergence of new three phases BLDC engines, embedded in the drive wheel opens a new perspective on their use in the vast majority of mechatronic systems using intelligent controlled displacement of the robots or mobile platforms. The big problem with these engines is for now the difficult interfacing with a microsystem, micorcomputer or computer. These motors have only one type of controller that only accepts analogue controls that are specific to the application area for which they were created (bicycles and electric scooters).

Otherwise, such an engine has a number of major advantages: direct drive, excellent power / volume ratio, precise speed control, less space than conventional ones, while delivering much better performance and reliability, IP64 protection, the axle of the wheel is firmly fixed and thus the connecting wires (both power and control) do not require rotating contacts, they do not have brushes which provide a much greater reliability.

The recent emergence of these three-phase BLDC engines has, as a secondary effect, a major internal and international market lack of finding adequated dedicated controllers.

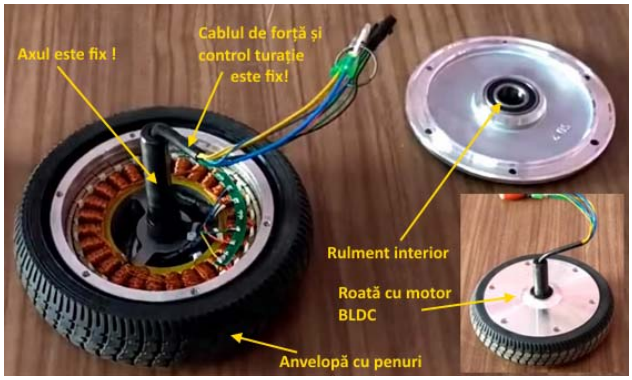

Figure 1. Brushless three-phase BLDC motor, integrated inside the wheel, a cutting-edge novelty in mechatronics

This is implicitly due to the great powers developed by the engines but especially because of the limited field for which they are used. Such motors with integrated wheel

construction (Figure 1) used in our security and surveillance robot have powers of about 180 watts at the 36 volt supply voltage. There is one type of controller (made in several versions of power and voltage) that are made to be driven directly by electromechanical control elements. Such a controller is the ZTECH E80030-B (Figure 2) controller capable of controlling motors with power up to 450W and supply voltages of 36V or 48V.

We were in a situation where we had a superb engine-driven controller but totally incompatible with the two micro-systems planned to work on the robot (Arduino and Raspberry Pi).

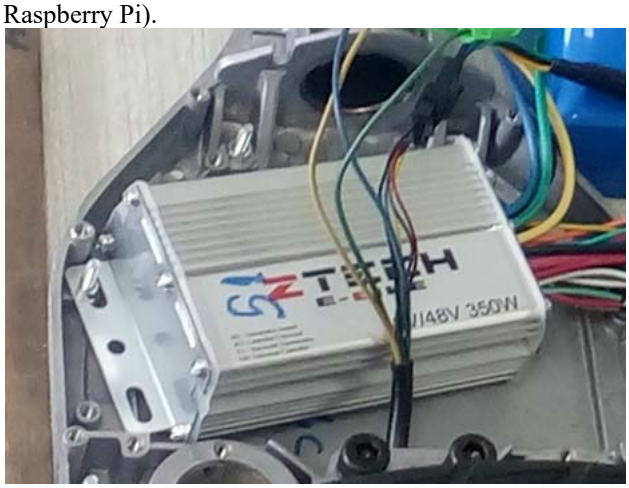

Figure 2. The ZTECH E80030-B controller, perfectly compatible with three-phase BLDC motors but not with the microsystem

Normally, the only solution was to design an Inteligent platform solving the interface problem between the computing microsystem and the ZTECH controller.

2. ORIGINAL PLATFORM FOR BLDC ENGINE CONTROLLERS AND CALCULATION MICROSISTEMS

Two methods were used to control the acceleration through the Arduino micro system. The first method consisted in the linear control of the engine's acceleration and deceleration and the second method in the stepwise control of both acceleration and deceleration. Although both methods have worked successfully, finally, the best version to be used was the one with linear acceleration and deceleration control due to better controllability of system movement.

For this method we used a potentiometric divider on one of Arduino's analog inputs. A 10 Kohm Joystick was used on Arduino's A1 analog input having the output directed to PWM 9 pin for the left drive group and another joystick on Arduino's analog A2 pin and the PWM 10 pin, for the right drive group. At the same time, each joystick also includes one button (without hold) which, when pressed, generates a 100 millisecond pulse to the ZTECH controller, effectively changing the direction of the corresponding motor (see the figure in Figure 3 shown in the Appendix at the end of the paper).

The model was used for field tests under difficult conditions even though the final chassis was not ready. We had to use only 4 wheels (Figure 4) of which only 2 having powered engines (in the final version there will be 6 motor driven wheels, in 3 and 3 mode, track type traction).

Tests have shown that the chassis can be successfully controlled even in this form, the two wheels have enough power to move smoothly with loads of about 90 kilograms in addition to the robot's momentary weight.

As shown in Figure 3 (shown in the Appendix at the end of the paper) the control joysticks are taken over by the Arduino computer microsystem, which using the associated software generates PWM signals at outputs 9 and 10. Pulses modulated in duration requires an digital to analogue conversion that occurs at the channel level with T1, R1, R3, R5, C1 (right drive) respectively T2, R2, R4, R6, C2 transforming PWM signal into a linear voltage trip. This, through D1-D6 diodes, effectively drives the engine speed for each controller. The D1-D6 diodes also protect the command from any possible reverse feedback with possible signals from the controller.

Changing the direction of movement is done by activating the IDR (right channel) and IDS (left channel) microswitches placed on the Arduino input pins 3 and 2 respectively. The control software sends the commands to the Arduino pins 4 (right wheels) and 5 (left wheels) and actuate a relay actuator module that will crimp the ND contacts for 100 milliseconds of the two white wires of the controller (the reversing wires). Relays have been used to ensure galvanic decoupling between the device and the controller.

Arduino powee rquirements use step-down CC / CC voltage regulators (36Vcc stepped down to 9,7Vcc)..

The tests generated minor changes in the final software, making linearizations specific to each trip of potentiometers in the joysticks, and implementing reversal comutation time to the optimal value of 100 milliseconds.

Finally, the softeare version loaded in the Arduino micro system is shown below:

```
int pwmPinS = 9; /* pin iesire de tip PWM conectata la canal FET Stanga*/
int inPinS = 1; /* tensiune de comanda conectata la pinul Analog 1, de exemplu un potentiometru 0-2.48V excursie*/
int valS = 0; /* variaba citire STÂNGA*/
float voltS = 0; /* variaba tine intermediar STÂNGA*/
int pwmPinD = 10; /* pin iesire de tip PWM conectata la canal FET Dreapta*/
int inPinD = 2; /* tensiune de comanda conectata la pinul Analog ,2 de exemplu un potentiometru 0-2.48V excursie*/
int valD = 0; /* variaba citire DREAPTA*/
float voltD = 0; /* variaba tine intermediar
```

```
DREAPTA*/

    int KEYinD = 2; // Buton schimba sens DREAPTA
    int KEYinS = 3; // Buton schimba sens STANGA
    void setup(){
      TCCR1B = TCCR1B & 0b11111000 | 0x02;
      pinMode(4, OUTPUT);          // setez pin digital 4 ca iesire releu Stanga
      pinMode(5, OUTPUT);          // setez pin digital 4 ca iesire releu Dreapta
    pinMode(pwmPinS, OUTPUT); /* setam Pinul 9 PWM ca pin de iesire FET Stanga*/
      pinMode (KEYinD, INPUT);
      pinMode (KEYinS, INPUT);
      Serial.begin (9600);
    }
    void loop()
    {
      int buttonValD, buttonValS;
      buttonValD = digitalRead (KEYinD);
      buttonValS = digitalRead (KEYinS);
        if (buttonValD == HIGH){
      digitalWrite(4, HIGH);          // dezactiveaza releu Dreapta
      }
      else{
       digitalWrite(4, LOW);            // activeaza releu Dreapta
        delay(100);
      }
      if (buttonValS == HIGH){
       digitalWrite(5, HIGH);          // dezactiveaza releu Stanga
      }
      else{
        digitalWrite(5, LOW);       // activeaza releu Stanga
        delay(100);
      }
    /*  citeste valoarea pe pinul de intrare de la potentiometru Stanga*/
    valS = analogRead(inPinS);
    /*  citeste valoarea pe pinul de intrare de la potentiometru Dreapta*/
    valD = analogRead(inPinD);
    voltS =valS * 0.04 + 30;
    voltD =valD * 0.04 + 30;
    valS = voltS;
    valD = voltD;
    analogWrite(pwmPinS, valS);
    analogWrite(pwmPinD, valD);
```

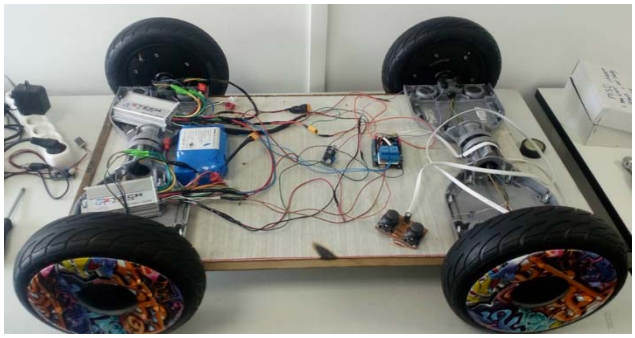

Figure 4. The simple four-wheel test chassis, of which only two are driven, has been used to finalize the final parameters of the command and control software

The driving wheel platform in the final version (6-wheel) is ready to be mounted to the final chassis model that is still in work, not being yet finished. The software and hardware modules have proven they can consistently control the BLDC-type wheels and are a new, innovative and modern solution, adaptable to any of today's robotic platforms.

Another inconvenience to the ZTECH controller is that the change of direction of the rotaton of the wheel is done without being signaled. Even if the schematic of Figure 59 performs the switching in a firm and correct manner at each actual driving direction, practically we also felt the need to indicate the state of the direction of rotation of the wheels (also visual and as a possible proccesed signal).

This has generated a new type of both optical and electric signaling sensor/actuator of the travel direction parameter (Figure 5 and Figure 6). Basically, the command taken over the left (Arduino 5) and right (Arduino pin 4) is taken over by two separate signaling channels. Thus, the directional shift signal from Arduino pin 5 is taken over by the transistor T1 which receives a positive pulse of 100 milliseconds and causes the Rel1s relay to be clamped by closing a Normal Open contact for 100 milliseconds.

The relay is mainly used as a galvanic separation element and control for the next stage of the transistor group T2 and T3. This circuit controls a load (consisting of R5 and LeftLed1) which switches cyclically on and off, depending on the number of pulses received from the K1s contact of the Rel1s relay. The first push will turn on the LED and the second will turn off the LED.

At start-up, both EC junctions of the transistors are closed and do not consume energy (thus saving the system's batteries) so the LED is off. In this state, the C3 capacitor is charged by load and R4. When K1s switches to the contact position, the voltage on C3 is discharged on the gate of T3 and opens it by turning on Led1. At the same time T2 opens through R2 forcing the gate of T3 with positive voltage keeping firmly open. C3 is discharged through R4 and T1.

The next command given by K1s C3 is downloaded through the T3 gate by first closing T3 and then T2. The R3 resistance is the gate of T3 in 0 stopping the led. The process resumes cyclically indicating forward rotation when the led is off and the rotating reversed rotation of the robot motors when the led is on.

If we want to transmit the direction of movement to the operator, we now have access to an electrical signal that can be detected, transmitted, processed or compared to any desired analog or digital system (voltage variaton on T3 Source pin).

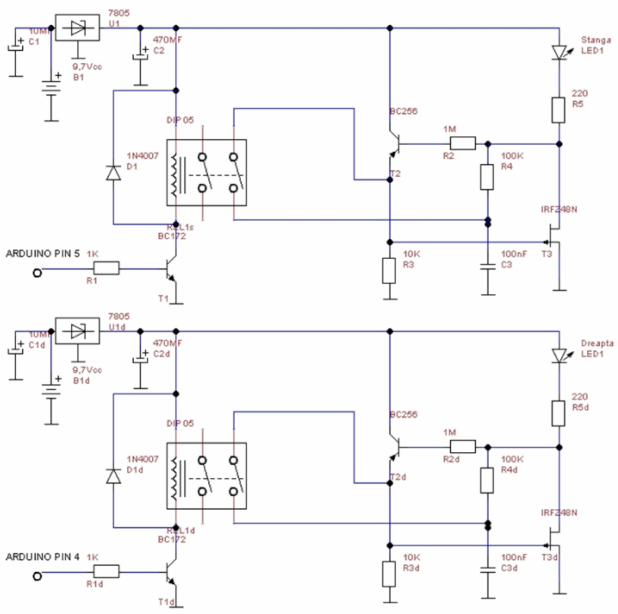

Figure 5. Optical and electric signaling system of engine rotation direction change (dual channel)

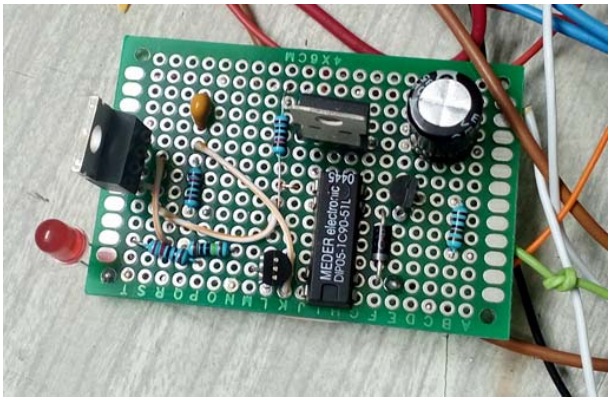

Figure 6. The mono channel optical and electric signaling system in the test phase

We get an excellent platform wich resolve the interfacing between a computing system (of any kind) with the ZTECH controller thus opening the door to mechatronic applications to the new three phase BLDC electric motor.

3. CONCLUSIONS

An intelligent platform that opens interesting horizons in any application where the controlled system performs travel using wheels. The system is particularly suited to where high power consumption is desired with optimal consumption and low volume. The test model (Figure 4) has only a third of the final power of our robot, but has managed to move a man without difficulty (90 Kg) in normal travel. An aspect that opens up new perspectives that can be exploited in the final project, namely the possibility of actually carrying at least one injuried person, which is imminent danger (depending on the situation on the site), to the location where the command and control station of the robot is placed.

REFERENCES

[1] Eben Upton and Gareth Halfacree, *Raspberry Pi User Guide 2nd Edition,* John Wiley & Sons Ltd., The Atrium, Southern Gate, Chichester, West Sussex, PO19 8SQ, United Kingdom, 2014.

[2] Matt Richardson and Shawn Wallace, *Getting Started with Raspberry Pi.* Published by O'Reilly Media, Inc., 1005 Gravenstein Highway North, Sebastopol, CA 95472, United States of America, 2013.

[3] Cay Horstmann and Rance D. Necaise, *Python for Everyone,* John Wiley & Sons Ltd., The Atrium, Southern Gate, Chichester, West Sussex, PO19 8SQ, United Kingdom, 2014.

[4] Gheorghe Ion GHEORGHE, Anghel CONSTANTIN, Sergiu DUMITRU, Microingineria Mems & Nems Inteligente, Editura CEFIN, București, Romania, 2013.

[5] Gheorghe Ion GHEORGHE, Adaptronica Sistemelor Inteligente, Editura AGIR, București, Romania, 2014

[6] Y.Daniel Liang, *Introduction to Java Programming 8-th edition,* Pearson Higher Education. Upper Saddle River, New Jersey, 07458, 2011.

[7] Roland Siegwart, Illah Reza Nourbakhsh, Davide Scaramuzza, *Introduction to Autonomous Mobile Robots*, Massachusetts Institute of Technology, MIT Press, 2011.

ANNEX

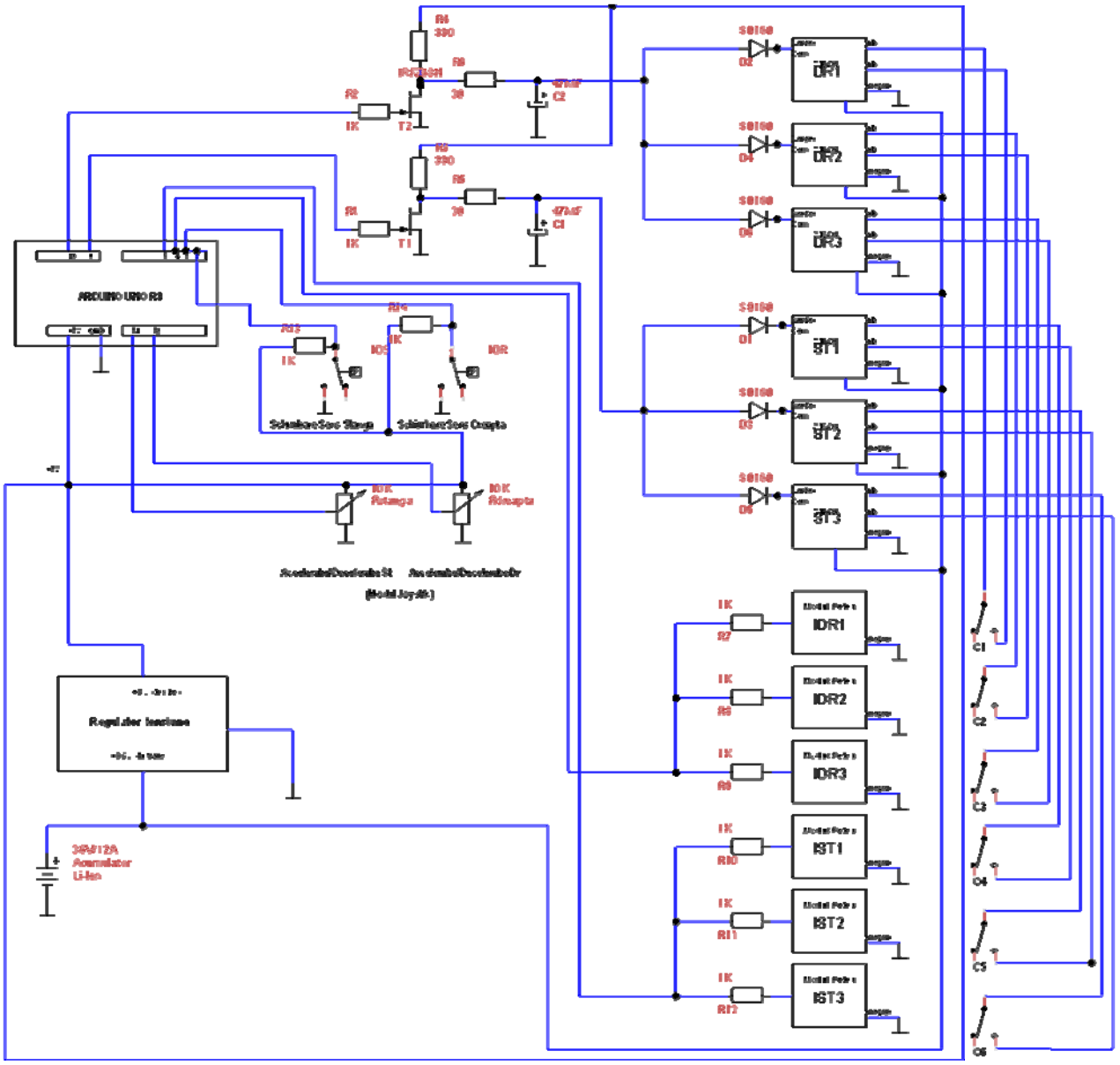

Figure 3. The final final assembly diagram for the platform controlling all 6 wheels, including the rotation direction shifting system

The Scientific Bulletin of VALAHIA University
MATERIALS and MECHANICS –Vol. 16, No. 15

DOI 10.1515/bsmm-2018-0016

3D COMPLEX STRUCTURES THROUGH FUSED DEPOSITION MODELING AS A RAPID PROTOTYPING TECHNOLOGY DESIGNED FOR REPLACING ANATOMIC PARTS OF HUMAN BODY

Nastase-Dan CIOBOTA[1], Gheorghe GHEORGHE [2]

[1] National Research & Development Institute for Non-Ferrous and Rare Metals - I M N R
102 Biruintei Blvd., PANTELIMON, jud ILFOV, 077145, ROMANIA

[2] National Institute of Research and Development in Mechatronics and Measurement Technique (INCDMTM), 6-8 Sos. Pantelimon, Bucharest

E-mail: dan_ciobota@yahoo.com

Abstract: *The paper aims to demonstrate the capability of FDM – Fused Deposition Modeling 3D printing technique to build complex structures designed for replacing anatomic parts of human body. It proposes to push the limits of FDM machine in order to achieve both structural integrity, mechanical properties and complexity of the 3D print part. Main applicability focus on bioengineering - developing new, lightweight implants but also can easily extended to airspace/automotive industry.*

Keywords: *rapid prototyping, CAD/CAM/CAE, Fused Deposition Modeling, 3D structures*

1. INTRODUCTION

We started from the idea of the innovative and very much interest from researchers at the present time, to create porous structure (see Figure 1), able to integrate the new tissue, resorbed in the new implant.

This represents a major challenge for researchers working in the field of tissue engineering and developing materials capable of accelerating biocomposite repairing defect. In this way, it reduces both the time and the costs in terms of rehabilitation patients.

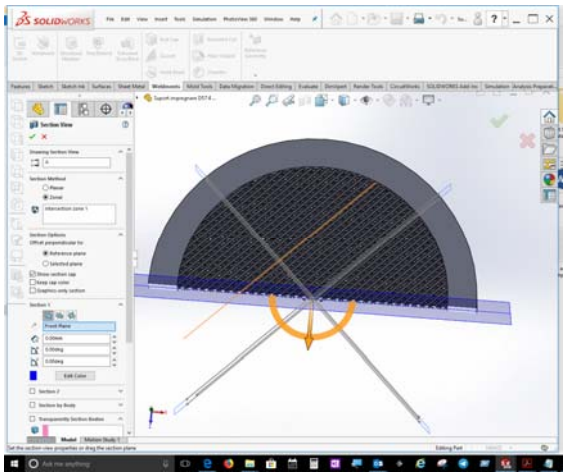

Figure 1. Porous structure Design in SolidWorks 2018

For initial tests it has chosen a structure of interwoven, with successive layers arranged in an order of 45 degrees in one another (see Figure 2).

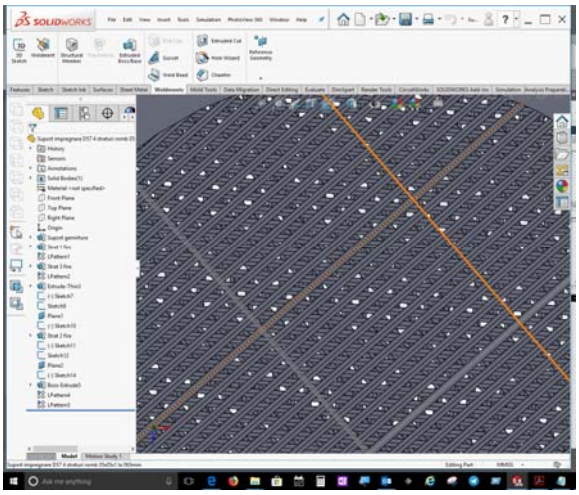

Figure 2. Emphasizing the lattice structure

2. Material used: Polyether-ether-ketone -PEEK

This semi-crystalline thermoplastic product is based on Polyether-ether-ketone resin. It is very advanced technologically and is characterized by a combination of outstanding mechanical properties and temperature resistance, excellent resistance to chemicals.

Features:

- Excellent dimensional stability
- Hardly flammable and with self-extinguishing properties
- High resistance to high doses of radiation energy
- Good resistance to abrasion and wear
- Great value rigidity, resistance and elasticity
- High termoplasticity, applicability, good adhesive properties and weldability
- High dimensional stability at warm temperatures
- The high temperature continues stable
- Low coefficient of linear extension
- Good electrical insulation at different temperatures

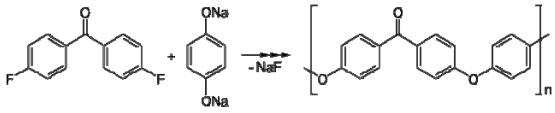

Figure 3. The chemical structure of PEEK

Polyether-ether-ketone (see Figure 3) is a colorless organic thermoplastic polymer that is part of the family of poliaril ether ketone, material used in engineering applications. It was introduced on the market by the firm Victrex PLC, then Imperial Chemical Industries (ICI) in the early 1980.

Polyether-ether-ketone polymer is obtained by stepwise polymerization.

2.1 Additive Manufacturing filaments deposit material. General aspects

In order to use the 3D material is pulled into the wires with a diameter of 1.75 mm (see Figure 4). This material shows excellent adhesion properties of successive layers, making it suitable for 3D printing processes.

Figure 4. Zortrax M200 FDM printer – compact design

3D printing is also known as computer modeling that can be executed through a variety of methods and can use different types of materials, but any of them lies the principle of creating layered (rising) of an object solid-the technology used to create layers. This process means creating real 3D model construction, computer-controlled. 3D digital model is saved in the file format STL (Standard Template Library) and is sent to be printed at 3D printer. Then 3D printer arranges the overlay layer after layer, thus forming the subject-matter. 3D printer is distinguished from ordinary printer. 3D printer produces print objects in 3D space. The 3D model is built on the path of overlapping layers of matter. This process is sometimes known as rapid prototyping and 3D printing.

Nowadays practically everything can be done in 3D printer: parts for the aviation industry, the production of models and prototypes in the field of industrial and technical creation of decorations and works of art, performances, architectural models with application in industry fashion, children's toys industry, food industry-medical, culinary, prostheses and manufacture of implants (fragments of skeleton, bones, cartilages). However the most complex objects can be executed only with the help of professional 3D printers, and these in turn are very expensive.

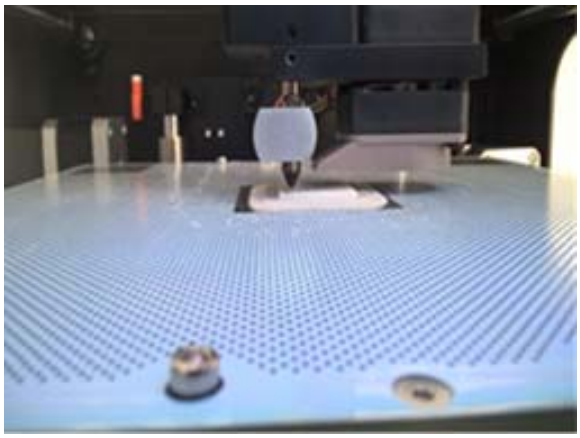

Figure 5. The Print Extruder Head during the Fused Deposition Modeling process – in progress

2.2 Considerations related to the orientation of building objects in the work area of the machine

Continuing by presenting several considerations related to the orientation of building objects in the work area of the machine.

Steps to be followed for the manufacture of an object method in additive manner FDM:

- Obtaining three-dimensional virtual model of a items to be manufactured, and export/save it in format STL;
- STL import/open the file object in the software of the machine;

- STL object orientation in the work area of the machine (translation, rotation);
- The choice of process parameters for FDM;
- Layering sections, with planes parallel to each other and perpendicular to the direction of the building;
- Generating support structures (for example, file format: SSL-Stratasys Sections Language);
- Generate rows/paths of submission of filaments (file format. SML-Stratasys Machine Language);
- Transmission of the file to the FDM machine (see Figure 5, 6);
- The construction of the object through the overlapping layers of material;
- Post processing object (removal of surface processing support structure, etc.).

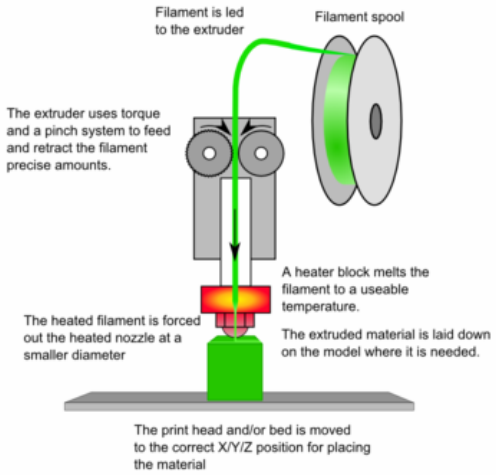

Figure 6. Schematic FDM principle

Choosing the optimal orientation of building represents one of the fundamental problems in the FDM (as in all processes of the additive manufacturing), significantly influencing different aspects such as the time and cost of construction, surface quality, dimensional precision and mechanical characteristics and shape, but also the volume of support structures and their position towards the object.

Decision as to the orientation of the building will be taken depending on the geometry and dimensions of the object, as well as other features dictated by the application for which it is manufactured, the experience of the operator having a very important role in this stage planning process.

For this reason, a good amount of time and research is being conducted in order to automate the selection of optimal orientation on the basis of certain criteria, so assuming collating information related to the specifics of the process and parameters of process, the geometry of the object and how the characteristics of manufactured objects are influenced by the orientation of the building, with then, the different techniques for optimizing the process (Figure 6).

2.3 Rules respected when designing parts made by additive manufacturing

What rules will be set out below (without being far from their claim exhaustiveness) builds on the experience of designers and users, on the recommendations of the manufacturers, as well as theoretical studies and tests aimed at determining the influence of specific process parameters values using the FDM (thickness of filament diameter sections, the distance between the rows of fabric, the filling layer styles), orientation or support structure, the capability to build parts with certain geometric shapes and sizes that meet at the same time one or more of the requirements listed above.

Moreover, should not be omitted that the objects have characteristics which depend on manufactured and machine model used and, in this sense being made and published benchmarking studies type. For example, a recent study assessed the machine from MakerBot CupCake company in terms of the precision of three-dimensional geometric and dimensional limitations, of geometric elements (holes, pockets, bosses of different shapes and sizes, thin walls, shear walls or geometry in the console), and geometric tolerances and repeatability. Also manufactured parts for Ultimaker machine and of the PLA, are given general geometric constraints, which should be taken into account in the design such that the mechanical properties are better in the x-y plane, or that horizontal wall thickness must not be less than 1 mm.

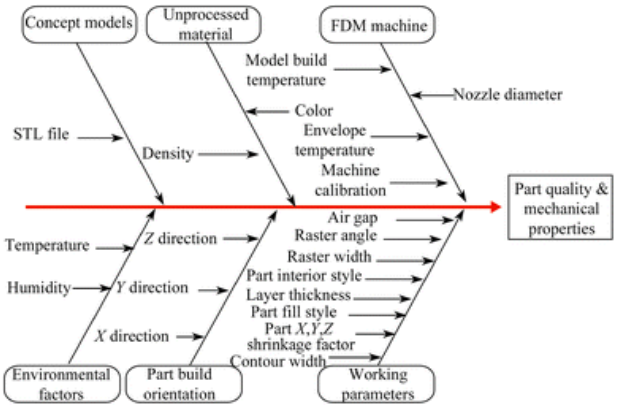

Figure 6. Optimization of FDM process

The manner in which the material, construction and orientation trajectory of the mechanical characteristics and deposition influences the quality of the play areas are analysed and in [9]. These studies were developed as part of a larger project at the University of Paderborn from Germany, hereinafter referred to as "Direct Manufacturing Design Rules", which takes into account the definition of rules for standard items (plates, items in the console, thin walls etc.) from parts that are manufactured using three types of additive

manufacturing processes including FDM (using Fortus, machine building materials: ABS and Ultem).

There are being studied the mechanical properties of FDM, being listed several rules for designers and operators:

- to choose the orientation of the building, to ensure the acquisition of loading traction along the layer and not perpendicular to it. It should also be kept in mind that compression resistance of FDM is almost double compared to the tensile strength;
- increased mechanical strength and rigidity can be obtained giving a negative value parameter that sets the distance between the rows of material;
- to pay attention to the design of the connected edges of the parts, because there are tensioners in these areas because of the incomplete filling caused by the filament discontinuity;
- since the shear resistance between the layers is greater than that between the rows, if the final piece is subject to such a stress, its orientation during manufacture has to be made accordingly.

2.4 Advantages and disadvantages of STL format
STL format, summarizing the advantages are as follows:

- Allows an easy conversion, STL format containing only a list of plane triangles, very simple coding, to be read and verified;
- It is independent of CAD system used to model virtual object;
- Admitting a wide variety of input data, three-dimensional representations which can be converted into B-rep triangular representations;
- Provides simple algorithms for slicing, due to the way of representation through a network of triangles, operations performed on the specimen being simple and precise;
- Offers the possibility of sharing model, useful when the work area of the machine of the additive manufacturing is not large enough, the object being divided into several parts and assembled from individually constructed.

Weaknesses of STL format refers to the following:

- Areas approximated curves through triangular facets, with negative implications on the quality of the surfaces;
- STL file size is large and very large, due to the redundancy format;
- Geometric errors of the type: goals (missing triangles), triangles which intersect, duplicate, inconsistent or normal degenerated faces;
- Does not allow the inclusion of metadata or other requirements regarding micro texture, structure or multiple materials (information necessary in view of new developments in certain additive manufacturing processes).

3. CONCLUSIONS

Thermoplastic filaments are versatile materials perfect for 3D printing prototypes which can be used in thorough tests before starting the production processes. It exhibits a high level of hardness, allowing to complete durable prints without compromises on their quality. With these materials, boldest models can acquire a unique, smooth, semimat surface and resemble elements manufactured with mass production plastics, therefore, imitate complete consumer products or end-use parts. These materials are also fully suited for creating prototypes of mechanical parts or casing elements for performance tests, medical and biomedical parts.

REFERENCES

[1] Fadel, G.M., Kirschman, C. (1996), Accuracy issues in CAD to RP translations, Rapid Prototyping Journal, Vol. 2 Iss: 2, pp.4 – 17.

[2] Mäkelä, I., Dolenc, A. (1993), Some Efficient Procedures for Correcting Triangulated Models, Solid Freeform Fabrication Symposium, Austin, Texas, p.126-134

[3] Jamshidi, P., Haddad, M., Mansour, S. (2005), A new database approach to improve STL files correction algorithms, 18th International Conference on Production Research.

[4] Li, J.-F., Zhong, Y.-X., Li, D.-S.: Research on errors identifying and repairing of STL file, Machinery Design & Manufacture (2), 40–42 (2002).

[5] Agarwala, M.K. ş.a., Structural quality of parts processed by fused deposition, Rapid Prototyping Journal, Vol. 2, Iss. 4, pp.4 – 19, 1996

[6] Ahn, S., Montero, M., Odell, D., Roundy, S., Wright, P., Anisotropic Material Properties of Fused Deposition Modeling ABS. Rapid Prototyping Journal, Vol. 8, No. 4, pp. 248 –257, 2002.

[7] Grimm, T., Fused Deposition Modelling: A Technology Evaluation, Time Compression Technologies, Vol. 2, No. 2, pp. 1-6, 2003.

[8] Lee, B.H., Abdullah, J., Khan, Z.A., Optimization of rapid prototyping parameters for production of flexible ABS object, Journal of Materials Processing Technology. Vol. 169, pp. 54–61, 2005.

[9] N. D. Ciobota, Standard Tessellation Language In Rapid Prototyping Technology, National Institute of Research and Development for Mechatronics and Measurement Technique, Bucuresti, The Scientific Bulletin of Valahia University – Materials and Mechanics – Nr. 7 (year 10) 2012.

[10] Fifth National Conference on Rapid Design, Prototyping and Manufacture, David Jacobson, Allan Rennie, Chris Bocking, John Wiley & Sons, 29 sept. 2004.

[11] https://www.manufacturingguide.com/en/fused-deposition-modeling-fdm.

The Scientific Bulletin of VALAHIA University
MATERIALS and MECHANICS –Vol. 16, No. 15

DOI 10.1515/bsmm-2018-0017

INTELLIGENT 4D MECHATRONIC MICROSYSTEM USED IN METROLOGICAL MEASUREMENT AND INTEGRATED CONTROL PROCESSES

Iulian ILIE[1], Gheorghe Ion GHEORGHE[1,2]

[1]National Institute of Research and Development in Mechatronics and Measurement Technique (INCDMTM), 6-8 Sos. Pantelimon, district 2, Bucharest, ROMANIA

[2]Valahia University of Targoviste – Faculty of Materials and Mechanical Engineering

E-mail: iuliancefin@yahoo.com, geocefin@yahoo.com

Abstract: *The smart mechatronic microsystem in 4D is designed and built for metrological and indstrial measurements and applications. The intelligent mechatronic system consists of 3 electric linear axes and a rotation system mounted on the linear Z-axis, which increases the capacity of the measuring and positioning system, allowing further expansion of the technical and technological services of the entire mecatronic system by connecting grippers, palpator, stylus module, etc.*

Keywords: *microsystem, 4D, metrological process, integrated measurement and control*

1. INTRODUCTION

Intelligent mechatronic microsystems used for measurement and positioning were firstly highlighted by the use of the term MEMS and NEMS in 1959 by Richard Feynman, by the issue of controlling and manipulating objects at micro and nano scales. Intelligent mechatronic microsystems are applicable in areas such as intelligent and automated manufacturing, environmental monitoring, medicine, aerospace, transportation, industry, communication, military technology, agriculture, etc. Intelligent mechatronic microsystems require manufacturing technologies to define small geometries, precise dimension control, flexibility monitoring, microcontroller interfacing, repeatability, reliability, high yield and low cost. MicronanoTechnologies together with Mecatronics, MicroMecatronics and NanoMecatronics develop the technological boundaries of complex processes.

The constructive and functional structure of the mechatronic and adaptronic systems comprises the fusion of elements and components of mechanical (precision mechanics), electronics (electronic circuits) and computer science (computers), in an architectural-functional system design of hardware and software, who assume in the same constructive purpose, the transfer of information, from the input to subsystems, of the "non-electrical" type, through analog-to-digital and digital-to-analogue transformations and amplifications.

There are different technological systems implemented with integrated control systems, for example:

a) The SCHAUBLIN 140-CNC (Figure 1) implemented with integrated control system is designed for individual or integrated manufacturing processes for parts in the mechatronics and micromechanics industry, high precision dimensioned in the manufacturing process through the integrated control system.

The technical performance of the integrated control systems corresponds to the technical requirements imposed by the parameters that characterize the reference mark and / or the exact tolerances imposed, in the present case: measuring range (X=1600mm; Y=400 mm; φ=360°), accuracy (on X= x: 0.01μm; on Y=0.002μm and on φ: 1'') and fidelity (for pentru φ: ±0.5'').

Figure 1. SCHAUBLIN 140-CNC

b) The STUDER 21 technology system (Figure 2) is integrated with the active and automated control system, it is intended for technological workshops and maintenance and testing laboratories for industrial / industrial parts executions / repairs / maintenance and measurements.

Figure 2. STUDER 21

c) The complex CNC technology system, type AGATHIN 150 SL 2 (Figure 3), is designed for microprocessing by centerless grinding, for small and very small industrial and very functional industrial parts of the micromechanics industry, the fine mechanics industry and mechatronics.

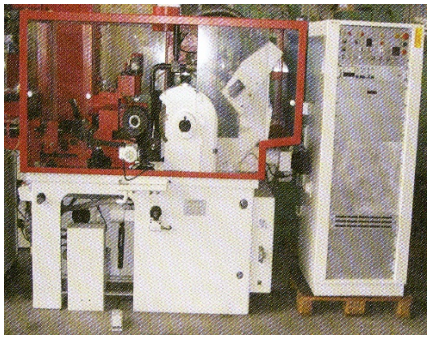

Figure 3. AGATHIN 150 SL 2

d) The ZEIRSCH + BALTRUSCH STARLINE 500 CNC Flatbed Technology System (Figure 4), integrated with the active and automated control system (specialized for "centerless"), is designed for the processing of high precision parts and used for assemblies precision and complex functions.

Figure 4. ZEIRSCH + BALTRUSCH STARLINE 500 CNC Flatbed Technology System

2. CONSTRUCTION OF THE INTELLIGENT 4D MECHATRONIC MICROSYSTEM USED IN METROLOGICAL MEASUREMENT AND INTEGRATED CONTROL PROCESSES

The intelligent 4D mechatronic microsystem used in metrological measurement and integrated control processes (Figure 5) is used in metrological measurement and integrated control processes designed for high precision linear measurements and high accuracy positioning of the parts, using telemonitoring and telecontrol.

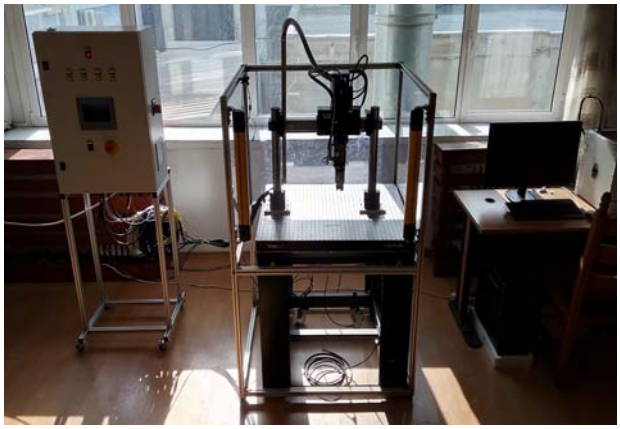

Figure 5. The intelligent 4D mechatronic microsystem used in metrological measurement and integrated control processes

The intelligent 4D mechatronic microsystem consists of: 4-coordinate XYZR, which allows precise positioning of the parts to be tested and analyzed; an ultra-precision 3D probe for measuring and controlling small and medium sized industrial parts; the anti-vibration table subsystem with horizontal leveling mechanism; integrated frame and transparent plastic protectors to protect the positioning and measurement process in the workspace; sensor barriers mounted on the integrated frame for securing the positioning and measuring process in the workspace; IP camera for viewing the mechatronic sub-system in 4D XYZR for telecontrol and telemonitoring; the control and control module; a central PC unit; PC monitor for displaying software and running programs via the PC central unit; router for connecting to cyber space and the parallel gripper designed for manipulating and positioning small and miniaturized parts and for ultra-precision 3D gripping / fixing.

The system consists of:

a) Subsystem of the anti-vibration table (Figure 6) on which the mechatronic elements are mounted.

The subsystem consists of a breadboard, self-leveling mechanism, mechanical frame, rollers for travel and adjustable support.

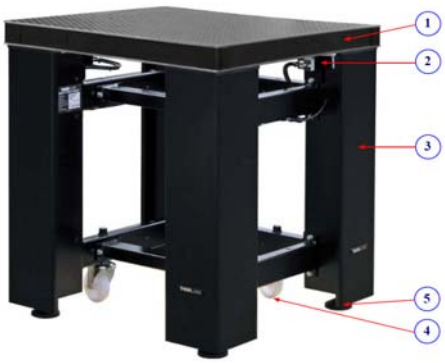

Figure 6. Subsystem of the anti-vibration table: 1- breadboard, 2- self-leveling mechanism, 3- mechanical frame, 4- rollers for travel, 5- adjustable support

b) Subsystem mechatronic intelligent 4D (Figure 7, position 2) mounted on subsystem of the anti-vibration table.

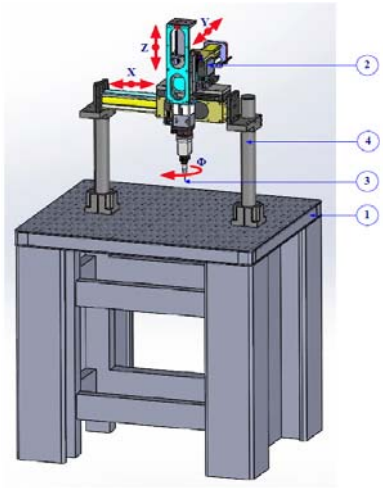

Figure 7. The experimental model of assemble: 1- subsystem of the anti-vibration table, 2- subsystem mechatronic intelligent 4D, 3- ultra-precision 3D probe, 4- adjustable support

The subsystem consists of electrical axis X, electrical axis Y, electrical axis Z, rotation axis and an electrical gripper.

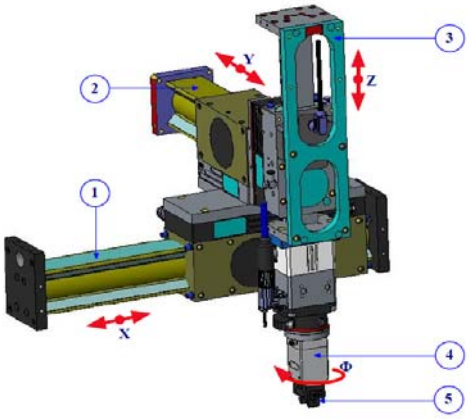

Figure 8. Subsystem mechatronic intelligent 4D: 1- electrical axis X, 2- electrical axis Y, 3- electrical axis Z, 4- axis for rotation Φ, 5- electrical gripper

The main technical data of electrical axis X, Y and Z are presented in table 1:

Table 1. Technical data of electrical axis X, Y and Z

ELECTRICAL AXIS	X	Y	Z
Stroke (mm)	200	100	100
Nominal force (N)	205	120	115
Repeat accuracy	±10μm		
Max. driving force (N)	500	250	250
Motor power	100W	50W	50W

The main technical data of axis for rotation Φ, are presented in table 2:

Table 2. Technical data of electrical axis for rotation Φ

ELECTRICAL AXIS Φ	Unit	Value
Weight	kg	1.2
Repeat accuracy	[°]	0.01
Rated / maximum torque	[Nm]	0.4/1.2
Max. rotational speed	[1/min	600

The main technical data of electrical gripper, are presented in table 3:

Table 3. Technical data of electrical gripper

Electrical gripper	Unit	Value
Stroke per jaw	[mm]	10
Min. / max. gripping force	[N]	40/140
Recommended workpiece weight	[kg]	0.7
Repeat accuracy	mm	0.02
Weight	[kg]	1.42
Max. permitted finger length	[mm]	64
Closing- / opening tim	[s]	0.6/0.6
Max. speed	[mm/s]	17

c) Subsystem ultra-precision 3D touch probe (Figure 9) for measuring and controlling small and medium sized industrial parts. Integration of the 3D touch probe is achieved through the technological fastening in the parallel gripper, the touch probe is connected to its own electronic module with a microcontroller.

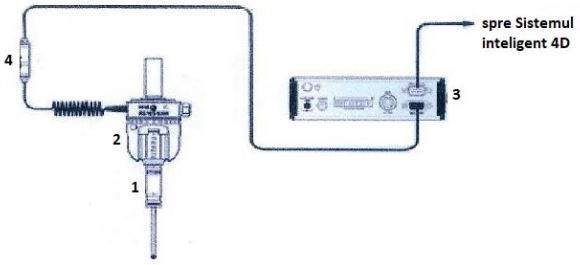

Figure 9. Subsystem ultra-precision 3D touch probe: 1- 3D stylus, 2- automatic fasteners, 3- electronic module with microcontroller, 4- connection cable

The main technical data of Subsystem ultra-precision 3D touch probe, are presented in table 4:

Table 4. Technical data of ultra-precision 3D touch probe

Subsystem ultra-precision 3D touch probe	Value/Unit
Gauging speed range	0.5 mm/s-80 mm/s
Trigger forces	0.002 N (2 gF) (at 50 mm stylus tip)
Trigger rate	5 triggers/s max
Sense directions	6 way: ±X, ±Y, ±Z
Probe length	43mm
Probe diameter	13.5 mm
Module pull-off force	800 g – 1000 g

All this components are controlled through dedicated controller. The command and control module is presented in Figure no. 10.

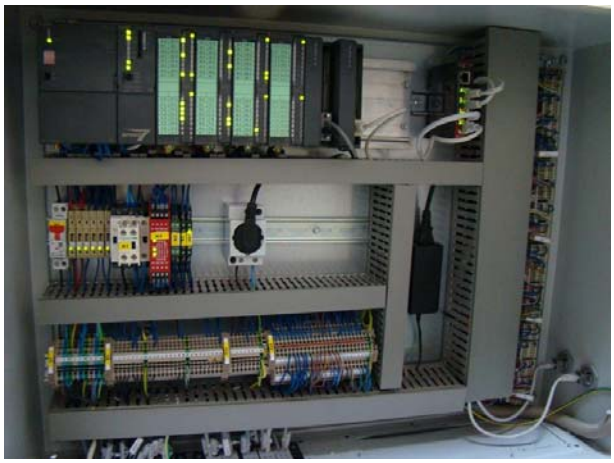

Figure 10. The command and control module

The smart mechatronic microsystem in 4D is protected through structural frame with bumpers (Figure 11) that can stop the processes if something goes in the work area. A smart IP camera is mounted on the structural frame for access and view the system from a different location, by connecting to a router and LAN/WAN. The smart mechatronic microsystem in 4D is connected to a PC and is controlled through a dedicated software.

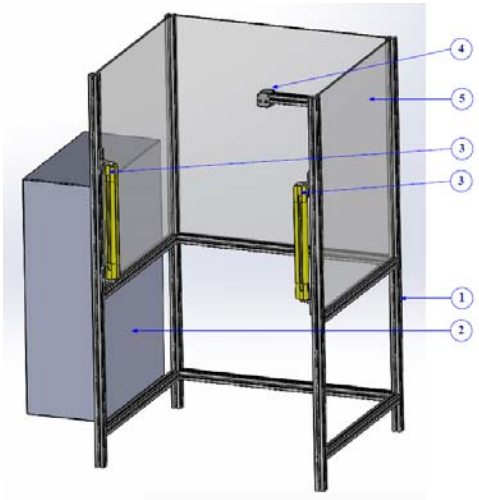

Figure 11. Structural frame with bumpers: 1- frame, 2- command and control module, 3- bumpers, 4- IP camera, 5- transparent plastic protective walls

3. CONCLUSIONS

The smart mechatronic microsystem in 4D is designed for ultra-accurate measurements and positioning, with the ability to remotely control it via a router, IP camera and internet, thus providing the telecontrol and telemonitoring feature.

Existing challenges will be maintained in the near future, and can be categorized into manufacturing challenges, assembly challenges, and implementation challenges. Without being able to create technologies that favor the creation and production of MEMS & NEMS systems through intelligent mechatronic microsystems, they will not be able to develop.

REFERENCES

[1] G. Gheorghe, "Cyber-MixMechatronics Engineering", Cefin Publishing House, 2016, ISBN 978-606-8261-24-9;

[2] G. Gheorghe, "Mechatronics & Cyber-Mechatronics Systems", Cefin Publishing House, 2015, ISBN 978-606-8261-22-5.

[3] G. Gheorghe, "Adaptronics Micro Nano Engineering", Cefin Publishing House, 2014, ISBN 978-606-8261-21-8;

[4] M. Silva, F. Pereira, F. Soares, et al., "An Overview of Industrial Communication Network, New Trends in Mechanism and Machine Science from Fundamentals to Industrial Applications", vol. 24, pp. 933-940, 2015, DOI:10.1007/978-3-319-03411-3-99.

[5] "Studiu și analiză privind concepțiile modelelor virtuale mecatronice și adaptronice și cyber-mecatronice și cyber-adaptronice" – Gh. I. Gheorghe, 2016, Editura CEFIN;

[6] "Elaborare noi concepte ştiinţifice şi tehnologice şi noi modele virtuale mecatronice şi adaptronice şi cyber-mecatronice şi cyber-adaptronice" - Gh. I. Gheorghe, 2016, Editura CEFIN;

[7] C. E. Pereira, S. Paladini, F. M. Schaf: Control and Automation Engineering Education: Combinig Physical, Remote and Virtual Labs, Proceedings of the 9th International Multi-Conference on Systems, Signals and Devices – SSD 2012, Chemnits, Germany, 20-23 March, pp. 1-10, 2012.

The Scientific Bulletin of VALAHIA University
MATERIALS and MECHANICS –Vol. 16, No. 15

DOI 10.1515/bsmm-2018-0018

NUMERICAL MODELING OF THE DYNAMICS OF THE MOTOR WHEEL.CASE OF ROLLING WITHOUT SLIDING

Vladimir Dragoş TĂTARU [1], Mircea Bogdan TĂTARU [2]

[1]University Valahia of Târgovişte, [2]University of Oradea

E-mail: vdtataru@gmail.com, btataru@uoradea.ro

Abstract: *The wheel is a very important machine part. It is very often found in the construction of the vehicles. Therefore its dynamics must be studied properly. In the paper is presented the dynamical survey of a wheel which climbs on an inclined plane under the action of an active moment produced by an engine. The case of rolling without sliding was taken under consideration in the paper. The approach of the problem is a numerical one. The differential equations describing the movement of the motor wheel were written in matrix form. The paper also presents a method of removing of the constraint forces from the differential equations of motion.*

Keywords: *dynamic study, numerical modeling, rolling, sliding*

NOMENCLATURE

$\overline{M_m}$ -motor couple acting upon the wheel

$\overline{F_r}$ -viscous damping force

$\overline{M_r}$ -viscous damping couple

$\overline{M_f}$ -couple of the rolling friction

s -friction rolling coefficient

$\overline{T}$ -sliding friction force

$\overline{N}$ -force of normal reaction

$\overline{G}$ -force of gravity

α –inclination angle of the plane

R –radius of the wheel

C_1 –mass center of the wheel

m –mass of the wheel

g –gravitational acceleration

J_{z_1} -axial moment of inertia

$v_{O_1x_1}$ -velocity of the point O_1 projection on the O_1x_1 axis

$v_{O_1y_1}$ -velocity of the point O_1 projection on the O_1y_1 axis

ω_{z_1} -angular velocity of the wheel

T_1 ($O_1x_1y_1z_1$)-body fixed reference frame

T (O x y z)-fixed reference frame

φ_1-angle of self-rotation of the wheel

c_t -viscous damping coefficient corresponding to the translational movement

c_r -viscous damping coefficient corresponding to the rotation movement

sgn –denotes signum function

T –denotes the transposition matrix operation

$\overline{k}$ -denotes the unit vector of the Oz axis

1. INTRODUCTION

We will consider a wheel supported on an inclined plane and acted upon by a system of forces and couples as it is shown in the figure bellow (Fig.1). We aim to perform the dynamics survey of this wheel namely that means its motion under the action of forces.

$$\overline{M}_f = -s \cdot N \cdot \mathrm{sgn}(\omega_{z_1}) \cdot \overline{k}$$

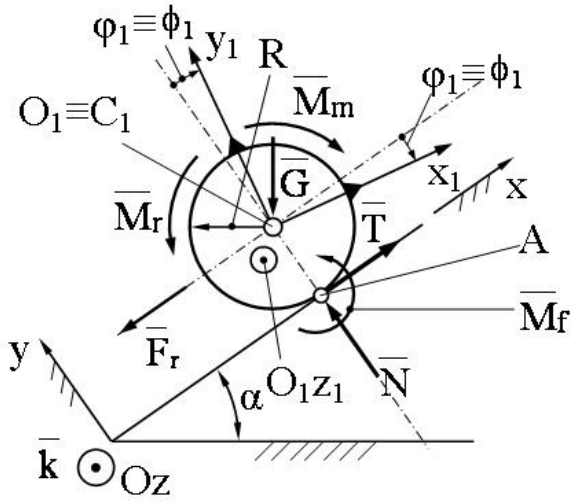

Figure 1. Motor wheel

2. WRITING DIFFERENTIAL EQUATIONS OF MOTION

The differential equations describing the movement of the motor wheel may be written in projections on the axis of the body fixed reference frame under the following matrix form [1-17]:

$$\mathbf{M}_{O_1} \cdot \dot{\mathbf{v}}_1 = \mathbf{Q}_g + \mathbf{Q} + \mathbf{Q}_c \tag{1}$$

$$\dot{\mathbf{x}}_1 = \mathbf{R}_1 \cdot \mathbf{v}_1 \tag{2}$$

In the relationships (1) and (2) the terms involved may be written as follows:

$$\dot{\mathbf{v}}_1 = \left[\dot{v}_{O_1x_1} \;\vdots\; \dot{v}_{O_1y_1} \;\vdots\; \dot{\omega}_{z_1}\right]^T \tag{3}$$

$$\mathbf{v}_1 = \left[v_{O_1x_1} \;\vdots\; v_{O_1y_1} \;\vdots\; \omega_{z_1}\right]^T \tag{4}$$

$$\dot{\mathbf{x}}_1 = \left[\dot{x}_{O_1} \;\vdots\; \dot{y}_{O_1} \;\vdots\; \dot{\varphi}_1\right]^T \tag{5}$$

$$\mathbf{M}_{O_1} = \left[\begin{array}{c:c:c} m_1 & 0 & 0 \\ \hdashline 0 & m_1 & 0 \\ \hdashline 0 & 0 & J_{z_1} \end{array}\right] \tag{6}$$

$$\mathbf{Q} = \mathbf{Q}_a + \mathbf{Q}_r \tag{7}$$

In the relations (3-5) the exponent "T" indicates the transposition matrix operation. The torque of the active forces relatively to the origin O_1, in projections on the body fixed reference frame T_1 ($O_1x_1y_1z_1$) may be written as follows:

$$\mathbf{Q}_a = \mathbf{R}_1^T \cdot \mathbf{Q}_a^0 \tag{8}$$

In the relation (8) the quantities involved have the following expressions:

$$\mathbf{R}_1 = \left[\begin{array}{c:c:c} \cos(\varphi_1) & -\sin(\varphi_1) & 0 \\ \hdashline \sin(\varphi_1) & \cos(\varphi_1) & 0 \\ \hdashline 0 & 0 & 1 \end{array}\right] \tag{9}$$

$$\mathbf{Q}_a^0 = \left[-m \cdot g \cdot \sin(\alpha) \;\vdots\; -m \cdot g \cdot \cos(\alpha) \;\vdots\; M_m\right]^T \tag{10}$$

The torque of the resistant forces relatively to the origin O_1, in projections on the body fixed reference frame T_1 ($O_1x_1y_1z_1$), may be written as follows:

$$\mathbf{Q}_r = -\mathbf{R}_1^T \cdot \mathbf{C} \cdot \mathbf{R}_1 \cdot \mathbf{v}_1 \tag{11}$$

In the relation (11) the matrix C has the following expression:

$$\mathbf{C} = \left[\begin{array}{c:c:c} c_t & 0 & 0 \\ \hdashline 0 & c_t & 0 \\ \hdashline 0 & 0 & c_r \end{array}\right] \tag{12}$$

The torque of the constraint forces in projections on the body fixed reference frame T_1 ($O_1x_1y_1z_1$) taking into account the moment of rolling friction $\overline{M_f}$, may be written as follows:

$$\mathbf{Q}_c = \mathbf{R}_1^T \cdot \mathbf{L}_{\lambda f 0} \cdot \boldsymbol{\lambda} \tag{13}$$

In the relations (13) the quantities involved have the following expressions:

$$\mathbf{L}_{\lambda f 0} = \left[\begin{array}{c:c:c} 1 & 0 & R \\ \hdashline 0 & 1 & -s \cdot \mathrm{sgn}(\omega_{z_1}) \end{array}\right] \tag{14}$$

$$\boldsymbol{\lambda} = \left[T \;\vdots\; N\right]^T \tag{15}$$

The torque of the gyroscopic forces in projections on the body fixed reference frame T_1 ($O_1x_1y_1z_1$) may be written in matrix form as follows:

$$\mathbf{Q}_g = -\tilde{\boldsymbol{\omega}} \cdot \mathbf{M}_{O_1} \cdot \mathbf{v}_1 \tag{16}$$

In the relation (16) the quantities involved have the followings expressions:

$$\tilde{\boldsymbol{\omega}} = \begin{bmatrix} 0 & -\omega_{z_1} & 0 \\ \omega_{z_1} & 0 & 0 \\ 0 & 0 & 0 \end{bmatrix} \tag{17}$$

The expressions of $\mathbf{v}_1$ and $\mathbf{M}_{O_1}$ are given by the relations (4) and (6) respectively.

3. EQUATIONS OF KINEMATIC CONSTRAINT

Between kinematical parameters of the rigid solid body the following constraint relations may be written:

$$\dot{x}_{O_1} + R \cdot \dot{\varphi}_1 = dx_{O_1} / dt + R \cdot d\varphi_1 / dt = 0 \tag{18}$$

$$\dot{y}_{O_1} = dy_{O_1} / dt = 0 \tag{19}$$

In the relations (18) and (19) x_{O_1} and y_{O_1} represent the coordinates of the origin O_1 relatively to the fixed reference frame T (O x y z). In matrix form relations (18) and (19) will be written together as follows:

$$\mathbf{L}_{\lambda 0} \cdot \dot{\mathbf{x}}_1 = \underset{2\times 1}{\mathbf{0}} = [0 \mid 0]^T \tag{20}$$

In the relationship (20) the quantities involved have the following expressions:

$$\mathbf{L}_{\lambda 0} = \left[\begin{array}{c|c|c} 1 & 0 & R \\ \hline 0 & 1 & 0 \end{array}\right] \tag{21}$$

$$\dot{\mathbf{x}}_1 = \left[\dot{x}_{O_1} \mid \dot{y}_{O_1} \mid \dot{\varphi}_1\right]^T \tag{22}$$

Using the relationship (2), the relationship (20) may be written in the following equivalent form:

$$\mathbf{L}_\lambda \cdot \mathbf{v}_1 = \underset{2\times 1}{\mathbf{0}} = [0 \mid 0]^T \tag{23}$$

In the relation (23) the expression of the column matrix v_1 is given by the relation (4) and the matrix L_λ has the following expression:

$$\mathbf{L}_\lambda = \mathbf{L}_{\lambda 0} \cdot \mathbf{R}_1 \tag{24}$$

In the relation (24) the expression of the matrix $\mathbf{R}_1$ is given by the relation (9). If we derive the expression (23) with respect to time we will obtain:

$$\mathbf{L}_\lambda \cdot \dot{\mathbf{v}}_1 + \dot{\mathbf{L}}_\lambda \cdot \mathbf{v}_1 = \underset{2\times 1}{\mathbf{0}} = [0 \mid 0]^T \tag{25}$$

In the relation (25) the expression of $\dot{L}_\lambda$ is given by the following relation:

$$\dot{\mathbf{L}}_\lambda = \mathbf{L}_{\lambda 0} \cdot \dot{\mathbf{R}}_1 = \mathbf{L}_{\lambda 0} \cdot \mathbf{R}_1 \cdot \tilde{\boldsymbol{\omega}}_1 \tag{26}$$

In the relation (26) the expression of $\tilde{\boldsymbol{\omega}}_1$ is given by the relation (17).Using the relation (26) the relation (25) becomes:

$$\mathbf{L}_\lambda \cdot \dot{\mathbf{v}}_1 + \mathbf{L}_{\lambda 0} \cdot \mathbf{R}_1 \cdot \tilde{\boldsymbol{\omega}}_1 \cdot \mathbf{v}_1 = \underset{2\times 1}{\mathbf{0}} \tag{27}$$

Using the relation (24) the relation (27) becomes:

$$\mathbf{L}_\lambda \cdot \dot{\mathbf{v}}_1 + \mathbf{L}_\lambda \cdot \tilde{\boldsymbol{\omega}}_1 \cdot \mathbf{v}_1 = \underset{2\times 1}{\mathbf{0}} \tag{28}$$

The relation (28) may be written under an equivalent form as follows:

$$\mathbf{L}_\lambda \cdot \dot{\mathbf{v}}_1 = -\mathbf{L}_\lambda \cdot \tilde{\boldsymbol{\omega}}_1 \cdot \mathbf{v}_1 \tag{29}$$

In the next chapter we will present a method of eliminating the constraint forces from the differential equations of motion.

4. ELIMINATION OF CONSTRAINT FORCES FROM THE DIFFERENTIAL EQUATIONS OF MOTION

Constraint forces are unknown and therefore they must be removed from the differential motion equations. This section presents a method of eliminating the constrained forces from the differential equations describing the movement of the motor wheel. The differential equations of motion (1) may be written under the following equivalent form:

$$\mathbf{M}_{O_1} \cdot \dot{\mathbf{v}}_1 = \mathbf{Q}_1 + \mathbf{L}_{\lambda f} \cdot \boldsymbol{\lambda} \tag{30}$$

In the relation (30) the quantities involved have the following expressions:

$$\mathbf{Q}_1 = \mathbf{Q} + \mathbf{Q}_g \tag{31}$$

$$\mathbf{L}_{\lambda f} = \mathbf{R}_1^T \cdot \mathbf{L}_{\lambda f 0} \tag{32}$$

We will multiply the differential equation (30) to the left by the matrix $\mathbf{M}_{O_1}^{-1}$ and the relation becomes:

$$\dot{\mathbf{v}}_1 = \mathbf{M}_{O_1}^{-1} \cdot \mathbf{Q}_1 + \mathbf{M}_{O_1}^{-1} \cdot \mathbf{L}_{\lambda f} \cdot \boldsymbol{\lambda} \tag{33}$$

We will multiply the differential equation (33) to the left by the matrix $\mathbf{L}_\lambda$ and we will obtain:

$$\mathbf{L}_\lambda \cdot \dot{\mathbf{v}}_1 = \mathbf{L}_\lambda \cdot \mathbf{M}_{O_1}^{-1} \cdot \mathbf{Q}_1 + \mathbf{L}_\lambda \cdot \mathbf{M}_{O_1}^{-1} \cdot \mathbf{L}_{\lambda f} \cdot \boldsymbol{\lambda} \tag{34}$$

Taking into account the relation (29) the relation (34) becomes:

$$-\mathbf{L}_\lambda \cdot \tilde{\boldsymbol{\omega}} \cdot \mathbf{v}_1 = \mathbf{L}_\lambda \cdot \left(\mathbf{M}_{O_1}^{-1} \cdot \mathbf{Q}_1 + \mathbf{M}_{O_1}^{-1} \cdot \mathbf{L}_{\lambda f} \cdot \boldsymbol{\lambda}\right) \tag{35}$$

In the relation (35) we will introduce the following notations:

$$\mathbf{L}_\lambda \cdot \tilde{\boldsymbol{\omega}} \cdot \mathbf{v}_1 = \mathbf{A} \tag{36}$$

$$\mathbf{L}_\lambda \cdot \mathbf{M}_{O_1}^{-1} \cdot \mathbf{Q}_1 = \mathbf{B} \quad (37)$$

$$\mathbf{L}_\lambda \cdot \mathbf{M}_{O_1}^{-1} \cdot \mathbf{L}_{\lambda f} = \mathbf{D} \quad (38)$$

Using the notation given by the relations (36-38), the relation (35) may be written as follows:

$$-\mathbf{A} = \mathbf{B} + \mathbf{D} \cdot \boldsymbol{\lambda} \quad (39)$$

The constrained forces may be determined from matrix equation (39) as follows:

$$\boldsymbol{\lambda} = -\mathbf{D}^{-1} \cdot (\mathbf{A} + \mathbf{B}) \quad (40)$$

Finally a system of six differential equations system with six unknowns will be obtained. The system will be written as follows:

$$\mathbf{M}_{O_1} \cdot \dot{\mathbf{v}}_1 = \mathbf{Q}_1 + \mathbf{L}_{\lambda f} \cdot \boldsymbol{\lambda} \quad (41)$$

$$\dot{\mathbf{x}}_1 = \mathbf{R}_1 \cdot \mathbf{v}_1 \quad (42)$$

The system given by the relations (41) and (42) will be solved using numerical integration methods.

5. NUMERICAL APPLICATION

Using MATLAB software a computing program which solves the differential equations system was designed. The computing program contains the following input data:

$$m_1 = 1\,[kg] \quad (43)$$

$$J_{z_1} = 1\left[kg \cdot m^2\right] \quad (44)$$

$$R = 1\,[meter] \quad (45)$$

$$c_t = 1\,[kg/\sec.] \quad (46)$$

$$c_r = 1\,[kg \cdot m/\sec.] \quad (47)$$

$$g = 10\left[metres/\sec.^2\right] \quad (48)$$

$$M_m = -12.5\ [N \cdot meter] \quad (49)$$

$$\alpha = \pi/6\,[radians] \quad (50)$$

$$s = 0.6\ [meters] \quad (51)$$

In order to integrate the differential equations system, the following initial conditions are necessary:

$$v^0_{O_1x_1} = 0\,[meters/\sec.] \quad (52)$$

$$v^0_{O_1y_1} = 0\,[meters/\sec.] \quad (53)$$

$$\omega^0_{z_1} = 0\,[radians/\sec.] \quad (54)$$

The initial values of the coordinates x_{O_1} and y_{O_1} of the origin O_1 relative to the fixed reference frame T (O x y z) are the followings:

$$x^0_{O_1} = 0\,[meters] \quad (55)$$

$$y^0_{O_1} = 0\,[meters] \quad (56)$$

The initial value of the self-rotation angle φ_1 is the following:

$$\varphi^0_1 = 0\,[radians] \quad (57)$$

The dynamic study was performed for a period of ten seconds. The results are presented in the figures below (Fig.2-5).

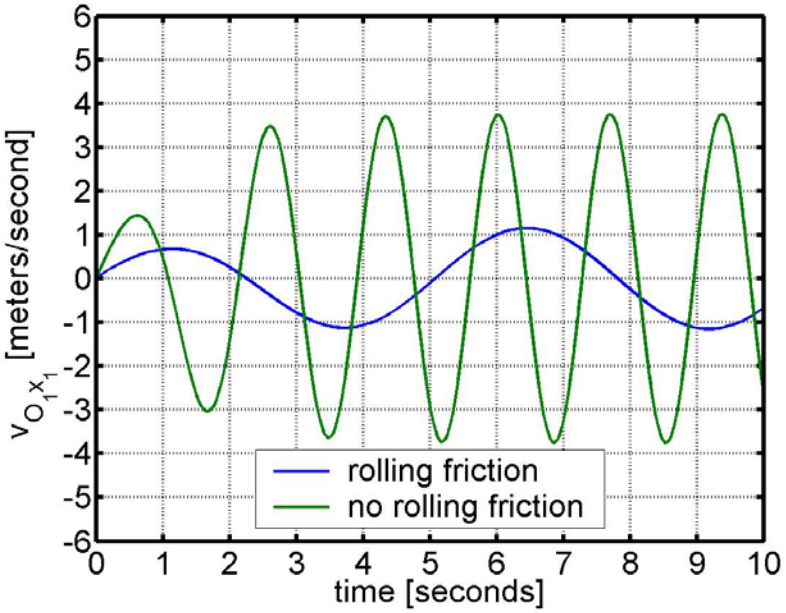

Figure 2. Variation of the velocity $v_{O_1x_1}$ with respect to time

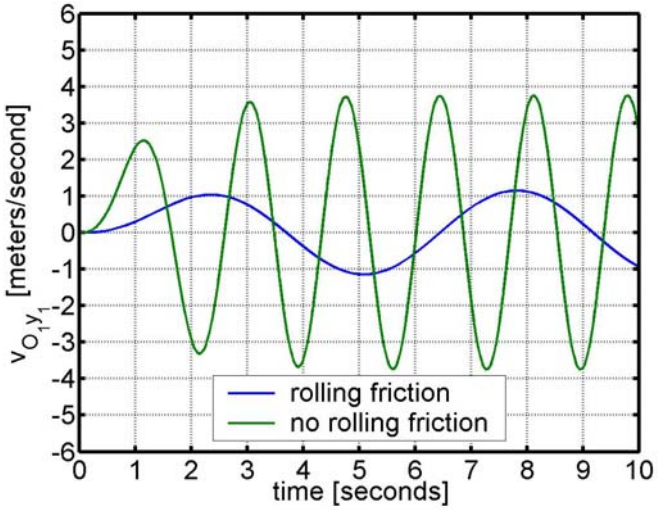

Figure 3. Variation of the velocity $v_{O_1y_1}$ with respect to time

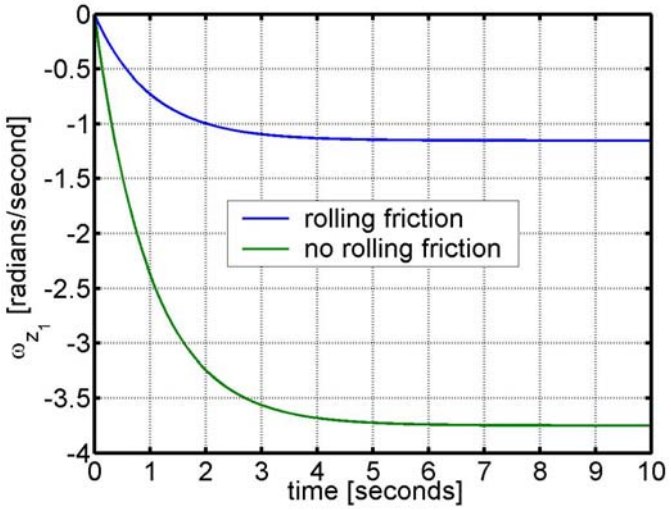

Figure 4. Variation of the angular velocity ω_{z_1} with respect to time

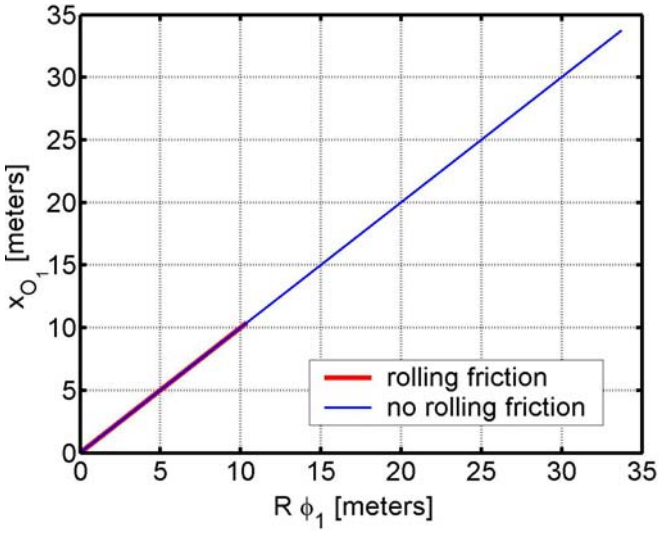

Figure 5. Variation of x_{O_1} abscissa with respect to the product $R \cdot \varphi_1$

The dynamics of the wheel was performed taking into account two distinct cases. In the first case the rolling friction has been taken under consideration by its effect, namely, the rolling friction moment $\overline{M}_f$. In the second case the rolling friction moment was ignored. Both results are presented in the above mentioned figures (Fig.2-5). In the figure 5 it is presented the variation of the abscissa x_{O_1} relative to the product between the radius of the wheel and the angle of self-rotation φ_1 which is supposed to be expressed in radians. The results presented in the figure 5 put into evidence the motion of pure rolling of the wheel taken under consideration. In other words the wheel rolls along the inclined plane and does not slide.

6. CONCLUSIONS

A dynamics survey from a numerical point of view has been presented in the paper. The differential equations which characterize the motion of a rigid solid body was written under a matrix form. In this way the MATLAB software elaboration was more easily. Using the numerical method presented in the paper we will obtain the values of all kinematical parameters for each moment of the wheel movement. In other words we will obtain the evolution in time of the position, velocity and acceleration of the wheel. The paper also presents an original method of constraint forces removing from the differential equations describing the movement of the motor wheel. This method is a very easy one because it is no more necessary to determine first the matrix expression of the orthogonal complement [10, 11] or natural orthogonal complement [5]. A determination method of constraint relations between kinematical parameters it is also presented in the work. The dynamic study may be continued with the determination of the values of the constrained forces for each moment of the movement.

REFERENCES

[1] Vâlcovici V., Bălan Şt., Voinea R., Mecanica Teoretică, Bucureşti, Editura Tehnică, 1968.

[2] Voinea R., Voiculescu D., Ceauşu V., Mecanica, Bucureşti, Editura Didactică şi Pedagogică, 1983, pp.351-355.

[3] Ştefan Staicu, Aplicaţii ale calculului matriceal în mecanica solidelor, Bucureşti, Editura Academiei R.S.R, 1983.

[4] Kamman J.V., Houston R.L., Dynamics of Constraint Multibody Systems, 1984, ASME, Journal of Applied Mechanics, volume 51, pp. 899-903.

[5] Jorge Angeles, Sang Koo Lee, The Formulation of Dynamical Equations of Holonomic Mechanical Systems Using a Natural Orthogonal Complement, Journal of Applied Mechanics, March 1988, volume 55 pp. 243-244.

[6] Houston R.L., Methods of Analysis of Constrained Multibody Systems, 1989, Mechanics of Structures and Machines, volume 17, No.2, pp. 135-143

[7] Nikraves P.E., Systematic Reduction of Multibody Equations of Motion to a Minimal Set, 1990, International Journal of Non-Linear Mechanics, volume 25, pp. 143-151.

[8] Papastravidis J.P., Maggi's Equations of Motion and the determination of Constrained Reactions, 1990, AIAA Journal of Guidance, Control and Dynamics.

[9] J.G. Papastavridis, On the Transitivity Equations of Rigid-Body Dynamics, Journal of Applied Mechanics, 1992, volume 59 pp. 955-962.

[10] W. Blajer, A Projection Method Approach to Constrained Dynamic Analysis, September 1992, Journal of Applied Mechanics, volume 59 pp. 643-649.

[11] W. Blajer, D. Bestle, W. Schiehlen, An Orthogonal Matrix Formulation for Constrained Multibody Systems, June 1994, Journal of Mechanical Design, volume 116 pp. 423-428.

[12] S.D. Mușat, Ecuaţii de tip Euler pentru solidul rigid deduse din ecuatiile lui Lagrange, 1995, A XIX-a Conferinţă de Mecanica Solidelor, volume 2 pp. 219-226.

[13] Ştefan Staicu, Mecanica Teoretică, Bucureşti, Editura Didactică şi Pedagogică R.A., 1998.

[14] Florin Bauşic, Mecanica Teoretică. Dinamica. Mecanica Analitică., Bucureşti, Editura Conspress, 2004.

[15] Wojchiech Blajer, On the Determination of Joint Reactions in Multibody Mechanisms, 2004, Journal of Mechanical Design, volume 126, pp. 341-350.

[16] Polidor Bratu, Mecanica Teoretică., Bucureşti, Editura Impulse, 2006.

[17] Staicu Şt., On the Determination of Joint Reactions in Multibody Mechanisms, September, 2009, Multibody Systems Dynamics, Springer, volume 22, No.2, pp. 115-132.

The Scientific Bulletin of VALAHIA University
MATERIALS and MECHANICS –Vol. 16, No. 15

DOI 10.1515/bsmm-2018-0019

RESEARCHES ON INERTIAL MECHATRONIC MOTION ANALYSIS SYSTEMS, BASED ON MEMS

Cristian Radu BADEA

National Institute of Research and Development in Mechatronics and Measurement Technique (INCDMTM), 6-8 Sos. Pantelimon, Bucharest, ROMANIA

E-mail: adresacontact@gmail.com

Abstract: *The aim of this paper is to provide an introduction into the inertial motion analysis field, focusing its attention on the analysis that is performed using modern mechatronic inertial motion capture systems, highlighting both the advantages and drawbacks of using such a system and outlining the main constituent elements of these systems as well as the necessary steps to be carried out in order to be able to accomplish such analysis.*

A modern mechatronic inertial motion analysis system's evolution it's based on MEMS (Micro-Electro-Mechanical-Systems) sensory network, each of which contains a combination of accelerometer, gyroscope, magnetometer. The signals from these MEMS are processed, by a microcontroller, using advanced algorithms in order to provide accurate data regarding body's segments kinematics, global positioning and magnetic field. Those data are being transferred to a biomechanical model for the analysis.

Despite its tremendous advantages, such as portability and real-time analysis capabilities, over alternative motion analysis systems, such as optical or mechanical systems, that based on external transmitters and/or video camera networks, restricting their use to special laboratory conditions and/or large workspace, mechatronic inertial systems are not based on an external infrastructure, they present a major disadvantage, namely the positional drift. The estimation of the human subject body's segments positions and orientation, absolutely requires an initial calibration procedure, called „sensor to segment calibration", that starts from the positional and orientation information received from the MEMS network, which are then transferred onto a biomechanical (scaled) model of the human body.

Keywords: *mechatronic inertial motion analysis system, MEMS, portability, real-time analysis, sensor to segment calibration, contact points, scenarios, positional drift*

1. INTRODUCTION

The aim of this paper is to provide an introduction into the inertial motion analysis field, focusing its attention on the analysis that is performed using modern mechatronic inertial motion capture systems, highlighting both the advantages and drawbacks of using such a system and outlining the main constituent elements of these systems as well as the necessary steps to be carried out in order to be able to accomplish such analysis.

A modern mechatronic inertial motion analysis system's evolution it's based on the evolution of sensors from the initial phase of individual sensory elements to MEMS (Micro-Electro-Mechanical-Systems) sensory network phase. Each inertial MEMS contains a combination of accelerometer, gyroscope, magnetometer and in some cases barometer, whose signals are processed, by a microcontroller, using advanced algorithms in order to provide accurate data regarding body's segments kinematics, global positioning and also regarding the atmospheric pressure and magnetic field. Those data are being transferred to a biomechanical model.

These modern mechatronic inertial motion analysis systems provide real-time working capabilities, having the latency around 30ms and wireless communication. They also provide a sampling frequency and a update rate, which is a new approach to sensors signal processing, meaning that the MEMS's signal is sampled at very high frequencies (100Hz) and since the data cannot be transmitted wirelessly at this frequency, because, in this case, the frequency is around of 100Hz and we still need to maintain a high accuracy, those signals, from MEMS, are being stored and transmitted in an incremental form. If a wireless communication interruption occurs, the data is temporarily stored, by a central sensory unit, within the MEMS and sent in full when the connection is restored. Usually the range of those wireless systems it's approx. 20-50m and the sampling frequency of MEMS is approx. 1000Hz, while the transmission it's performed at a frequency between 60-240Hz.

According to their specifications, these modern mechatronic inertial motion analysis systems are providing immunity to magnetic distortion, due to an extremely important function, called Magnetic Field Mapper that allows for MEMS to be placed onto

ferromagnetic surfaces (such as MEMS placed onto prosthetic areas, or props made of metal).

In the past decade, mechatronic inertial motion capture systems have seen an increase in the number of applications in the field of motion analysis for medicine, ergonomics and sports.

Despite its tremendous advantages, such as portability and real-time analysis capabilities, over alternative motion analysis systems [1-2], such as optical or mechanical systems, that based on external transmitters and/or video camera networks, restricting their use to special laboratory conditions and/or large workspace [3-11], mechatronic inertial systems are not based on an external infrastructure, they present a major disadvantage, namely the positional drift. The estimation of the human subject body's segments positions and orientation, absolutely requires an initial calibration procedure, called „sensor to segment calibration", that starts from the positional and orientation information received from the MEMS network, which are then transferred onto a biomechanical (scaled) model of the human body. This calibration introduces errors that may affect performance as follows:

a) First of all, the sensor-segment calibration is typically obtained by asking the subject to stand in a predetermined position (see Fig.1), which may be „N" type (neutral pose) or "T" type (the posture in which the arms are raised and collinear, forming together with the rest of the body the letter "T"). Each of these two positions presents some advantages and disadvantages. The "N" posture, as the name calls it, is neutral and thus relatively natural and easy to obtain and maintain, while, in the case of the "T" posture, the coordinate system of each body segment is aligned with the common coordinate system, of the analysis system, this posture being more difficult to obtain from the point of view of collinearity of the arms and their perpendicularity on the trunk, but also more difficult to maintain, as it imposes a high level neuro-muscular control on behalf of the human subject under analysis. Also, the "T" posture allows for high accuracy in what concerns the position of the shoulders. There are some systems that are allowing the calibration with the subject positioned in the posture "A", which represents a compromise between the two above mentioned postures, being closer to the natural and easier to maintain, than the "T" posture and to the same extent allowing for a more precise scaling than the "N" posture.

The postural fluctuations of the human subject, subjected to analysis, are an important source of errors, since the predetermined positions imposed on it, during the calibration process, are difficult to control and maintain, even for short periods of time, leading to orientation errors which can exceed 5 degrees.

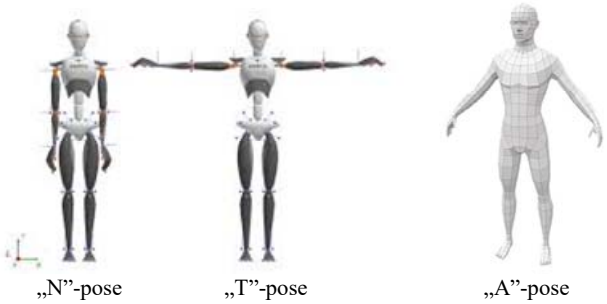

Figure 1. The calibration poses

b) Secondly, estimation of the orientation is done by processing the information received from the accelerometric sensors, the gyroscopic sensors and the magnetometer, included in the structure of each MEMS (by applying a KALMAN filter).

The overall accuracy of this type of motion analysis system is significantly affected by the electromagnetic distortions and calibration errors of MEMS's magnetometer.

c) Thirdly, the biomechanical model has limited accuracy when applied to a wide range of subjects. Model scaling imperfections and inaccurate estimates of MEMS's locations on body parts of the individual under analysis, are other sources of error affecting the overall precision.

The short-term changes in the orientation are captured accurately by the gyroscopic sensor, while the accelerometer and magnetometer sensors provide long-term stability. Precision depends both on the quality of sensor's calibration and on environmental conditions.

Tilt estimation may be distorted by long-term accelerations, while position estimation may be adversely affected by electromagnetic disturbances generated, for example, by the reinforcement present into the enclosure's walls, or neighboring electronic equipment.

In recent years, inductive motion analysis systems developers, have made special efforts to improve these systems, with efforts being particularly directed to overcoming the major sources of errors in these inertial systems to provide an accurate and consistent solution.

The most advanced inertial motion analysis systems, are combining the data received from the MEMS network, with advanced biomechanical models, the result of which its, especially, a decrease in sensitivity to the effects of magnetic distortion and in some cases even immunity to magnetic distortions ([12]).

Also, the sensor-segment calibration procedure is no longer based on data from the magnetometer, so the calibration can be done anywhere. Finally, although in the calibration action, the predefined posture ("N", "T" or "A") is assumed by the human subject, under analysis, along with a predefined pattern scaling,

advanced mechatronic inertial motion analysis systems allow the use of custom scaling models.

2. MECHATRONIC INERTIAL MOTION ANALYSIS SYSTEMS ARCHITECTURE

The vast majority of mechatronic inertial motion analysis systems are composed of a hardware subassembly and a software subassembly [2].

2.1 Hardware subassembly

The hardware subassembly its generally composed of a MEMS network, a system for fixing individual MEMS to the body of the subject, subjected to the analysis, a central sensory unit and a computing system (PC, laptop, tablet).

The hardware subassembly can be available in two configurations:

-wired configuration, where individual MEMS are connected, via electrical cables, to a central sensory unit. The latter has both the role of capturing signals from MEMS and sending them to a computing system, as well as powering each MEMS. The cumulative data received from the MEMS network can also be sent to the computing system, both, via electrical wires, or a wireless communication system, where these data are sent to the computing system via a wireless router;

-the wireless configuration, in which, each MEMS has its own power supply and its own wireless communication system, the data from them being wirelessly sent to central sensory unit, which is directly connected to the computing system.

In general, MEMS-based mechatronic inertial motion analysis systems, employ a number of 17 MEMS, positioned on the lower limbs (3 on the left lower limb and 3 on the right lower limb, one on each major segment, that is a part of each inferior member: the thigh, the tibia and the foot), the pelvis area (one on each side of the pelvis), on the upper limbs (three on each major segment, that is a part of each upper limb: palm, forearm and arm), head, sternum and posterior cervical / thoracic area. These MEMS contain, in the case of advanced mechatronic systems, a combination of at least three sensors:

- 3D gyroscope;
- 3D accelerometer
- 3D magnetometer.

Certain types of MEMS are also equipped with barometric sensors, such as those produced by Xsens.

The signals from the sensors, that are incapsulated inside each MEMS, are processed using a system-specific algorithm and then transmitted at relatively low frequencies (about 60Hz), but signal sampling precision is maintained at much higher frequencies (approx. 1kHz).

Besides this standard MEMS configuration, mechatronic inertial systems also allow the use of a number of additional MEMS, which can be placed on various props, which play a decisive role in the analysis (e.g.: Application of an additional MEMS, on a sword, in an analysis session of the movements involved in the manipulation of a sword).

Also, these mechatronic inertial mechatronic systems allow motion analysis to be performed with two or more human subjects (not restricted only to human subjects), without errors due to interference between MEMS networks, or due to interaction between the subjects involved, as they appear sometimes in the case of optical motion analysis systems.

Advanced mechatronic inertial motion analysis systems, based on MEMS, also allow for a motion capture session without the need for an uninterrupted connection (either through electrical wires or wireless) with a computing system, named independent session, in this case, the task of storing the captured motion information, is transferred to the central sensory unit, so that later, after this action is completed, the stored information to be sent towards the computing system in order to be further processed. The duration of a motion capture session, in this case, is limited by both the storage space allocated to this function and the capacity of the battery/batteries that feed the central sensory unit/individual MEMS. This additional capturing and storing function, of the central sensory unit, allows the use of these mechatronic inertial systems in a variety of environments (in narrow spaces, on stadiums, on rough terrain, in open field, or in a forest, etc.) and thus increases the degree of portability / autonomy of the system in question.

Although the system does not explicitly specify, because the central sensory unit has no user interface, in the case of mechatronic inertial systems that allow such independent sessions, it is absolutely necessary to do a sort of calibration at the beginning of each session, this consisting of adopting one of the previously mentioned postures and walking ten steps forth and ten back. After the capture session is completed, when the stored data is transferred towards the analysis software, in the software interface, the user has to choose the same calibration posture as the one adopted in the independent session.

Wireless mechatronic inertial motion analysis systems, based on MEMS, such as those produced by Xsens, contain a radio transceiver system that uses the bandwidth between 2.4-2.5KHz or the bandwidth between 5.2-5, 7KHz, which means that people who take part in the motion capture session are exposed to some level of radiation, but the power is very low, so the exposure does not pose a risk and is well below the internationally accepted safety level of radio frequency. These frequency bands comply with the ISM (Industrial, Scientific and Medical) standard, which is why, before starting an analysis session, the level of RF

protection of the medical devices, in the vicinity, must be checked to prevent interferences with it.

From the point of view of how MEMS are placed on the body of the human subject, that is subjected to the analysis, there are, at this time, two solutions:

- placing the MEMS on a belt-type fastening systems.

This positioning system has the advantage that the position of the individual MEMS can be easily adjusted at any point in time, thus allowing MEMS positioning, adaptable to the different requirements of each analysis;

Figure 2. The belts/straps system of Xsens, equipped with MEMS

- placing the MEMS in a predefined position on an over-elastic bodysuit, that molds on the user's body (see Fig.3). This positioning system has the advantage that the position of al the individual MEMS is always the same, no matter the number of consecutive session and also does not matter if the suit was initially removed and then reused - there in no need for a readjustment of the MEMS's positions, thus allowing the session to be repeated, under similar conditions, in this way reducing the total amount of time needed for the analysis process;

Figure 3. The Lycra-type bodysuit of Xsens, equipped with MEMS

2.2 Software subassembly

The software of a mechatronic inertial motion analysis system, based on MEMS, combines spatial positional data, received from MEMS, with a biomechanical human body model, that is specific to each software, in order to obtain the spatial positions of the digitally represented body segments. These kinds of software may have different uses (cinema-animation, video games, medicine, ergonomics, sports), which is why developers of such systems have created two dedicated solutions as follows:

- a solution dedicated to animation systems, especially used in cinematography, video games and virtual reality;

- a solution dedicated to motion analysis systems, especially used in medicine, sports and ergonomics.

The software of a mechatronic inertial motion analysis system, based on MEMS, allows real-time processing of information and digital representation, with milliseconds delays, which are only of a visual nature, the analysis process remaining unaffected. There are some software, such as Xsens's MVN Analyze, which allows for a reprocessing of information (post-processing), thus making it much more accurate than real-time processing. This post-processing, however, implies an increase in the analysis time and the need to use a computing system with superior performance in terms of data processing capacities.

Certain software, such as MVN Analyze, allows for the selection of motion analysis scenarios that differ in how the human subject interacts with the environment, making it easier to get the most accurate results:

- "*Single Level*" scenario, designed to be used in cases where the subject's interaction with the environment is conducted at a single level, for example at ground floor level. In this case, the contact points with the ground are assumed to be, on the OZ axis, equal to 0. Therefore, if this scenario is to be used in a stair climbing analysis, the height component is lost, each step being considered be positioned at ground level.

- "*Multi Level*" scenario, designed to be used in analysis that are taking place at different levels, such as stair climbing, sitting and lifting on/off the chair. This scenario, however, implies a small positive drift of the height component.

- "*Soft Floor*" scenario, designed to be used in analysis that are taking place on a single level, but the floor's surface is not rigid, it is compressible (such as a mattress in a training room), so the level shows some fluctuations in height.

- "*No Level*" scenario, designed for that kind of motion analysis, in which interaction with the floor does not matter. In this type of scenario, the pelvic area is considered fixed in space, all calculations being related to it. This scenario is especially recommended in the analysis of joint angles in biomechanics, or in activities

where contact with the soil cannot be fully defined, for example: skiing, skating.

This kind of system has some limitations, for example, the vertical changes, in a moving elevator scenario analysis, cannot be detected, as the contact points are linked to the elevator's floor, which gives the impression that the subject does not go up or down, but it stays at the same level.

3. MOTION CAPTURE USING A MECHATRONIC INERTIAL ANALYSIS SYSTEM

3.1 The general characteristics of a mechatronic inertial analysis system

Generally, a mechatronic inertial analysis system, based on MEMS, follows human body movements, represented by a biomechanical model consisting of 23 segments: the pelvis, the L5, L3, T12 and T8 spine segments, the neck, the head, the shoulders, the arms, the forearms, hands, thighs, tibia, feet and toes. Of these 23 segments, only 17 have an attached MEMS, the movements of those without an attached sensor are estimated by combining the information received from the 17 MEMS with the biomechanical model.

The kinematics of each body segment is relative to a local, common, Cartesian coordinate system, in which:

- the X axis is perpendicular to the frontal plane of the biomechanical model and has the positive direction determined by the rule of the right hand. This represents the depth coordinate of the interest point into the screen's plane. The X axis can be defined by the user during the calibration operation;

- the Y axis is perpendicular to the sagittal plane of the biomechanical model and has the positive direction determined by the rule of the right hand. This is the horizontal coordinate of interest point, into the screen's plane;

- the Z axis is perpendicular to the transverse plane of the biomechanical model and has the positive direction oriented towards the sky. This is the This is the vertical coordinate of interest point, into the screen's plane.

The coordinate system of each segment, of the biomechanical model, is constructed in such a way that, when the human subject, under analysis, adopts the "T" position, is aligned with the common, local, coordinate system described above.

Currently, mechatronic inertial motion analysis systems, based on MEMS, obtain the position and orientation of each segment relative to the local coordinate system, by means of complex fusion algorithms, applied to the acceleration, angular velocity and magnetic field, measured. The signals provided by the inductive sensor are complementary to the signals provided by the magnetic sensor and are therefore treated as such by the previously mentioned algorithms.

By integrating the angular velocity, as measured by the gyroscope sensor, an estimate of the orientation, of the segment in question, is obtained, but this can be affected by the integration errors. In order to obtain a time-stable estimation, the magnetic and gravitational components, obtained from the accelerometric and magnetic, sensors, are also taken into account, providing information about orientation and direction.

Estimation of the position is achieved by the double integration of the sensor's free acceleration, which is accurate for short periods of time, but it does not exhibit good stability over long periods of time, being particularly affected by orientation errors.

Combining an appropriate biomechanical model with advanced contact detection algorithms can lead to a correct estimate of the relative position and orientation of each segment as well as the overall body position relative to the environment.

Another source of error is the unstable contact between the MEMS and the body segment onto which it is placed, depending on the thickness and elasticity of the skin and/or the muscle layer (for example, it is preferable to place the MEMS onto the tibia's inner face, which has no muscles insertions, where the low thickness of the elastic tissue, meaning the skin, allows for increased stability, rather than the area of the calf, where the thickness of the elastic tissue, meaning the skin and the muscles, is high), as well as the quality of the possible fabric interposed between the subject's skin and MEMS.

The advanced, mechatronic inertial motion analysis systems, based on MEMS, allow the integration of force/pressure sensors into the analysis process, or to be combined with the optical or radiofrequency systems, to achieve more accurate results.

3.2 The calibration process of a mechatronic inertial analysis system

The calibration action is intended to estimate certain body dimensions of the human subject under analysis (which must also take into account the shoes sole thickness, if the human subject is equipped with shoes, during the analysis) and to estimate the orientation of the MEMS in relation to the body segments onto which they are placed (see Fig.4).

The origin of the segment is usually positioned in the proximal center of the joint, which is the functional rotation center.

The position of the anatomical elements is not directly measured, as in the case of optical analysis, but results from the processing of MEMS information regarding the accelerations, angular velocities and rotations, combined with the biomechanical model.

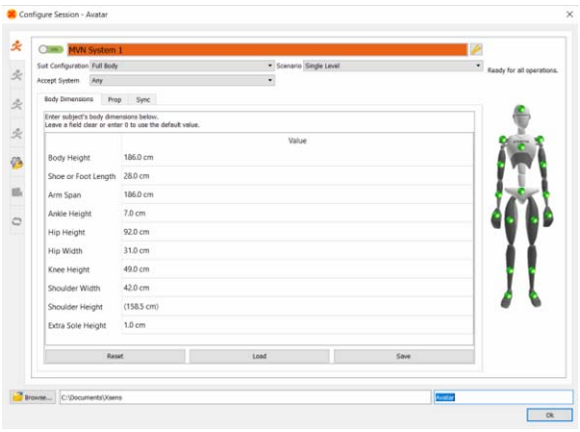

Figure 4. Calibration window

By measuring certain distances between the floor and/or certain anatomical skeletal protuberances, of the subject's body, the contact points with the environment and also the elements required for scaling the virtual dummy, are determined. The latter representing only an abstract visual representation of the human skeleton, in which certain bone segments are not individually represented, but grouped together with a well-defined body segment, such as: the thoracic cage is fixed together with the T8 vertebra, which has assigned the sternum's MEMS; the vertebrae are not directly measured, but are interpolated between the pelvis's, sternum's and head's MEMS, in accordance with a model of the spine and have joints located in the centers of rotation of the vertebrae. Similarly, the bone segments of the hand, neck and foot, are calculated and represented.

Rotation within a joint is currently defined by the orientation of the distal to the proximal segment.

The required dimensions of body segments, of the calibration are:

- the height of the ankle, is considered to be the distance from the ground to the center of the lateral malleolus;

- the height of the knee, is considered to be the distance from the ground to the center of the epicondyle lateral;

- the height of the hip, is considered to be the distance from the ground to the center of the great trochanter;

- the width of the hip, is considered to be the distance between the ante-superior iliac crests;

- arm span, is considered to be the distance from the tip of the middle finger of the right hand to the tip of the middle finger of the left hand;

- shoulder height, is considered as the distance from the ground to the acromion;

- shoulder width is considered as the distance between the right and left hand's acromion;

- foot length is considered to be the distance from the tip of the longest toe to the tangent with the heel;

- the height of the subject under analysis.

These dimensions are to be inputted into a user's interface window and used by motion analysis software to scale up the virtual model of the subject.

A very important function provided by some motion analysis software, such as MVN Analyzes, developed by Xsens, is to verify the proper activation and assignation of each individual MEMS on the body segment for which it is intended, because each MEMS has a unique assignment.

High performance mechatronic inertial motion analysis systems, allow the MEMS to be relocated if one of them is defective and needs to be replaced, or if a mistake has occurred in their positioning and a resumption of the entire operation is no wanted, although each of them has assigned a unique ID, that links them to a particular body segment, this being done by the user, by reallocation of the unique ID, within the MEMS activation and assignation identification window.

After the required measurements have been inputted and the activation and assignation, of the MEMS's, is verified, the next step in the calibration process is the estimation of each individual MEMS's position, on the corresponding body segments, also called "sensor-segment" calibration. For this, it is necessary for the subject under analysis, at first, to adopt one of the two previously mentioned positions ("N" or "T"), after which the subject must walk a number of steps forth and back. Within these postures, the positions of the body's segments are considered to be known and therefore it is necessary for the subject to maintains the imposed posture, as stable as possible, for a few seconds. The "N" posture is increasingly used in inertial motion analysis systems because it is considered to be "immune" to magnetic distortions.

Another faze of the calibration process is to define of the positive direction of the X axis. In the above-mentioned postures, the subject should be oriented towards the inside of the surface in which the analysis is carried out, which will determine the positive direction of the X axis, the origin of the common, local coordinate system, is to be considered as being positioned in the right heel. In the case of multi-subject analysis, this local coordinate system, previously mentioned, is a reference system for all subjects undergoing analysis. Also, in this case, it is necessary that all the subjects in question will have to start the calibration from the same place, eventually this place being represented by a mark on the surface on which the analysis will take place. However, most motion analysis software allows for subsequent change of direction and initial position.

4. CONCLUSIONS

Inertial motion analysis systems do not have an absolute positioning system, so spatial positioning errors will occur over time. For short sessions, these errors are in the order of centimeters, and in case of multi-subject sessions, the positions of the subjects can accumulate significant errors.

In order to minimize the positional drift, the analysis software uses the contact points between the subject under analysis and the environment, these being typically anatomical skeletal protuberances, considered to have the potential to interact physically with the environment, for example: the heel, the elbow, or the knee (see Fig.5).

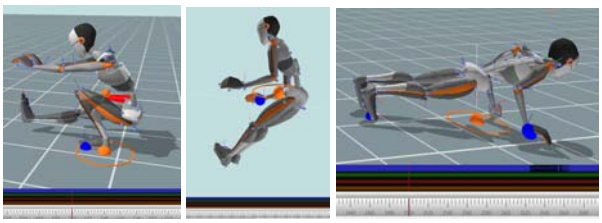

Figure 5. Contact points

Certain analysis software allows the user to visualize, in real-time, during motion capture, various motion charts, that are required (see Fig.6).

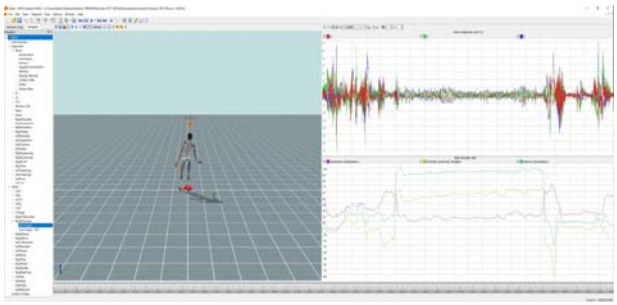

Figure 6. Real-time motion charts

In a Xsens's technical report, from March 2018, entitled "Consistent Tracking of Human Motion Using Inertial Sensing" [12] there were some extremely important conclusions regarding the quality of walking and running analysis, using the Xsens's inertial motion analysis system (composed of the MVN Link, the motion capture system and MVN Analyze, the motion analysis software), compared to the same walking and running analysis, conducted using the Qualisys optical capture system (which contains eight video cameras) and the OpenSim motion analysis software. The main conclusions are:

- the standard deviation of the angles, in the sagittal plane, between the inertial system produced by Xsens and the optical system composed of Qualisys and OpenSim, is less than 5 degrees, and for angles outside the sagittal plane, it is somewhat larger, due to the fact that OpenSim applies constraints to the angles of the knee and ankle and therefore does not make an estimate of these, outside the sagittal plane. If these constraints are removed, the correspondence of the values between these two systems is quite good;

- in the case of running, carried out over a period of 90 minutes, at different speeds and in conditions of significant electromagnetic disturbances, it was found that the angles of the ankle, knee and hip, obtained with the Xsens inertial system, are mostly corresponding, with those obtained with the optical system mentioned.

REFERENCES

[1] https://www.researchgate.net/publication/322441883_accuracy_between_optical_and_inertial_motion_capture_systems_for_assessing_trunk_speed_during_preferred_gait_and_transition_periods

[2] https://www.xsens.com/

[3] https://www.engadget.com/2014/07/14/motion-capture-explainer/

[4] https://www.motionshadow.com/biomech

[5] http://dynamicsystems.asmedigitalcollection.asme.org/article.aspx?articleid=1734670

[6] https://www.researchgate.net/publication/232703773_Kinematic_predictors_of_singleleg_squat_performance_A_comparison_of_experienced_physiotherapists_and_student_physiotherapists

[7] https://www.eumotus.com/blog/2018/01/09/motion-capture.html

[8] https://en.wikipedia.org/wiki/Motion_capture

[9] https://optitrack.com/support/

[10] https://teslasuit.io/blog/motion-capture/motion-capture-what-it-is

[11] https://ar-tracking.com/applications/motion-capture/

[12] Xsens MVN: Consistent Tracking of Human Motion Using Inertial Sensing, Technical Report, March 2018

The Scientific Bulletin of VALAHIA University
MATERIALS and MECHANICS –Vol. 16, No. 15

DOI 10.1515/bsmm-2018-0020

INCREMENTAL NUMERICAL METHOD USED FOR THE KINEMATICAL STUDY OF THE SLIDER-CRANK MECHANISM

Vladimir Dragoş TĂTARU [1], Mircea Bogdan TĂTARU [2]

[1]University Valahia of Târgovişte, [2]University of Oradea

E-mail: vdtataru@gmail.com, btataru@uoradea.ro

Abstract: *The kinematical study of mechanisms is a very important matter and therefore it must be done very properly. The slider-crank mechanism is very common in engineering applications. The present paper presents an incremental numerical method used for kinematical study of the aforementioned mechanism. The kinematics of the same mechanism is performed using an analytical method. In order to validate the incremental numerical method, the results obtained by using the two methods are then compared.*

Keywords: *mechanics, numerical incremental method, kinematical analysis*

NOMENCLATURE

$\underset{m\times n}{0}$ -zero matrix with “m” rows and “n” columns

φ_1, φ_2 -angles of self-rotation of the mechanism’s elements

$d\varphi_1, d\varphi_2$ -infinite small variations of the angles φ_1 , φ_2

$\Delta\varphi_1, \Delta\varphi_2$ -finite variations of the angles φ_1 , φ_2

Δt -increment of time

t_i -initial moment of the increment of time

t_{i+1} -final moment of the increment of time

φ_1^*, φ_2^* -values of the angles of self-rotation at a certain moment “t”

l_1 -length of the element “1” of the mechanism

l_2 -length of the element “2” of the mechanism

$T(Oxyz)$ -fixed reference frame

O -origin of the $T(Oxyz)$ fixed reference frame

$T_1(O_1x_1y_1z_1)$ -solid rigid “1” body fixed reference frame

O_1 -origin of the $T_1(O_1x_1y_1z_1)$ reference frame

$T_2(O_2x_2y_2z_2)$ -solid rigid “2” body fixed reference frame

O_2 -origin of the $T_2(O_2x_2y_2z_2)$ reference frame

$T_3(O_3x_3y_3z_3)$ -solid rigid “3” body fixed reference frame

O_3 -origin of the $T_3(O_3x_3y_3z_3)$ reference frame

1. INTRODUCTION

Kinematical analysis of any rigid solids system is a very important issue and for this reason it should be looked at with great care. The paper deals with the kinematical analysis of the slider-crank mechanism (Fig.1). It is made up of three elements linked together by joints and slides. The elements “1”, “2” and “3” are linked each other by cylindrical joints. These joints are denoted on the figure O_2 and O_3 .The element “3” of the mechanism is linked to the element which is considered to be fixed by a slide. The element “1” is linked to the fixed element by a joint. This joint is denoted on the figure by O_1 .The element “3” describes a translational motion. We aim ourselves to perform the kinematical study of this mechanism using an incremental numerical method and an analytical method. In other words we will perform a comparative kinematical study of the same mechanism. In order to validate the incremental numerical method, the results will be compared.

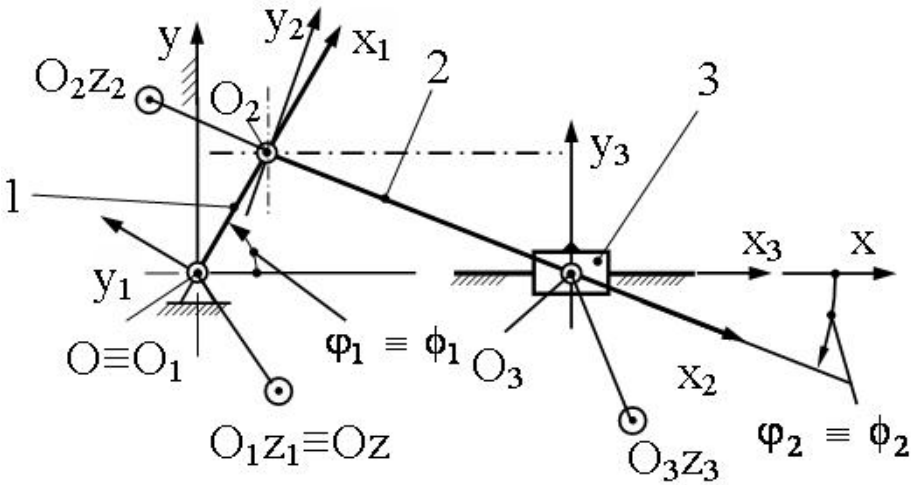

Figure 1. Slider-crank mechanism

2. KINEMATICAL ANALYSIS OF THE SLIDER-CRANK MECHANISM USING THE ANALYTICAL METHOD

In this paragraph, analytical relations will be established between positional parameter φ_1 and the position parameters of the other elements. In this situation the leading element is marked on the figure by O_1O_2 (Fig.1).The length of the element "1" is l_1 .The x_{O_2} , y_{O_2} coordinates may be expressed as a function of the φ_1 angle values as follows [1-16]:

$$x_{O_2} - l_1 \cdot \cos\varphi_1 = 0 \quad (1)$$

$$y_{O_2} - l_1 \cdot \sin\varphi_1 = 0 \quad (2)$$

Between the values of the x_{O_3} , y_{O_3} coordinates and the values of the φ_1 , φ_2 angles the following relationships may be written [2-4]:

$$x_{O_3} - l_1 \cdot \cos\varphi_1 - l_2 \cdot \cos\varphi_2 = 0 \quad (3)$$

$$y_{O_3} - l_1 \cdot \sin\varphi_1 - l_2 \cdot \sin\varphi_2 = 0 \quad (4)$$

The value of the y_{O_3} point O_3 ordinate (Fig.1) is equal to zero throughout the movement:

$$y_{O_3} = 0 \quad (5)$$

By solving the system consisting of equations (1-5) the following results will be obtained:

$$x_{O_2} = l_1 \cdot \cos\varphi_1 \quad (6)$$

$$y_{O_2} = l_1 \cdot \sin\varphi_1 \quad (7)$$

$$\varphi_2 = -\arcsin\left[(l_1/l_2)\cdot\sin\varphi_1\right] \quad (8)$$

$$x_{O_3} = l_1 \cdot \cos\varphi_1 + l_2 \cdot \sqrt{1-(l_1/l_2)^2 \cdot (\sin\varphi_1)^2} \quad (9)$$

$$y_{O_3} = l_1 \cdot \sin\varphi_1 - l_1 \cdot \sin\varphi_1 = 0 \quad (10)$$

3. KINEMATICAL ANALYSIS OF THE SLIDER-CRANK MECHANISM USING AN INCREMENTAL NUMERICAL METHOD

If we differentiate the relationships (1-5) with respect the φ_1 variable, the following results will be obtained:

$$dx_{O_2} + l_1 \cdot \sin\varphi_1 \cdot d\varphi_1 = 0 \quad (11)$$

$$dy_{O_2} - l_1 \cdot \cos\varphi_1 \cdot d\varphi_1 = 0 \quad (12)$$

$$dx_{O_3} + l_1 \cdot \sin\varphi_1 \cdot d\varphi_1 + l_2 \cdot \sin\varphi_2 \cdot d\varphi_2 = 0 \quad (13)$$

$$dy_{O_3} - l_1 \cdot \cos\varphi_1 \cdot d\varphi_1 - l_2 \cdot \cos\varphi_2 \cdot d\varphi_2 = 0 \quad (14)$$

$$dy_{O_3} = 0 \quad (15)$$

The relations (11-15) will be expressed using a single matrix relationship as follows:

$$A \cdot dq = B \cdot d\varphi_1 \quad (16)$$

In the relationship (16) the quantities involved have the following expressions:

$$\mathbf{A} = \left[\begin{array}{c|c|c|c|c} 1 & 0 & 0 & 0 & 0 \\ \hline 0 & 1 & 0 & 0 & 0 \\ \hline 0 & 0 & l_2 \cdot \sin\varphi_2 & 1 & 0 \\ \hline 0 & 0 & -l_2 \cdot \cos\varphi_2 & 0 & 1 \\ \hline 0 & 0 & 0 & 0 & 1 \end{array}\right] \quad (17)$$

$$\mathbf{dq} = \left[dx_{O_2} \;\vdots\; dy_{O_2} \;\vdots\; d\varphi_2 \;\vdots\; dx_{O_3} \;\vdots\; dy_{O_3}\right]^T \quad (18)$$

$$\mathbf{B}_1 = \left[-l_1 \cdot \sin\varphi_1 \;\vdots\; l_1 \cdot \cos\varphi_1\right]^T \quad (19)$$

$$\mathbf{B}_2 = \left[-l_1 \cdot \sin\varphi_1 \;\vdots\; l_1 \cdot \cos\varphi_1\, 0\right]^T \quad (20)$$

$$\mathbf{B} = \left[\mathbf{B}_1^{\mathrm{T}} \,\vdots\, \mathbf{B}_2^{\mathrm{T}}\right]^{\mathrm{T}} \tag{21}$$

Replacing the infinite small displacements by finite but small displacements the relation (16) becomes:

$$\mathbf{A}^* \cdot \Delta\mathbf{q} = \mathbf{B}^* \cdot \Delta\varphi_1 \tag{22}$$

In the relation (22) the quantities involved have the following expressions:

$$\mathbf{A}^* = \left[\begin{array}{c:c:c:c:c} 1 & 0 & 0 & 0 & 0 \\ \hdashline 0 & 1 & 0 & 0 & 0 \\ \hdashline 0 & 0 & l_2 \cdot \sin\varphi_2^* & 1 & 0 \\ \hdashline 0 & 0 & -l_2 \cdot \cos\varphi_2^* & 0 & 1 \\ \hdashline 0 & 0 & 0 & 0 & 1 \end{array}\right] \tag{23}$$

$$\Delta\mathbf{q} = \left[\Delta x_{O_2} \,\vdots\, \Delta y_{O_2} \,\vdots\, \Delta\varphi_2 \,\vdots\, \Delta x_{O_3} \,\vdots\, \Delta y_{O_3}\right]^{\mathrm{T}} \tag{24}$$

$$\mathbf{B}_1^* = \left[-l_1 \cdot \sin\varphi_1^* \,\vdots\, l_1 \cdot \cos\varphi_1^*\right]^{\mathrm{T}} \tag{25}$$

$$\mathbf{B}_2^* = \left[-l_1 \cdot \sin\varphi_1^* \,\vdots\, l_1 \cdot \cos\varphi_1^*\right]^{\mathrm{T}} \tag{26}$$

$$\mathbf{B}^* = \left[\mathbf{B}_1^{*\mathrm{T}} \,\vdots\, \mathbf{B}_2^{*\mathrm{T}}\right]^{\mathrm{T}} \tag{27}$$

From equation (22) it may be deduced:

$$\Delta\mathbf{q} = \left(\mathbf{A}^*\right)^{-1} \cdot \mathbf{B}^* \cdot \Delta\varphi_1 \tag{28}$$

By performing the calculations the following results will be obtained:

$$\Delta x_{O_2} = -l_1 \cdot \sin\varphi_1^* \cdot \Delta\varphi_1 \tag{29}$$

$$\Delta y_{O_2} = l_1 \cdot \cos\varphi_1^* \cdot \Delta\varphi_1 \tag{30}$$

$$\Delta\varphi_2 = -\left(l_1/l_2\right) \cdot \left(\cos\varphi_1^* / \cos\varphi_2^*\right) \cdot \Delta\varphi_1 \tag{31}$$

$$\Delta x_{O_3} = l_1 \cdot \left[\sin\left(\varphi_2^* - \varphi_1^*\right) / \cos\varphi_2^*\right] \cdot \Delta\varphi_1 \tag{32}$$

$$\Delta y_{O_3} = 0 \tag{33}$$

4. NUMERICAL APPLICATION

In order to validate the numerical the numerical incremental method, in this paragraph, a concrete numerical application will be presented. To do so, we will ascribe numerical values to the lengths of the mechanism elements and to the positional parameters of its elements. For analytical calculation, the variability interval of the independent variable must be first specified. This is denoted by' φ_1 "and represents the rotation angle of the leading element around the Oz axis. It is considered that the leading element describes two complete rotations around the Oz axis:

$$\varphi_1 \in [0,\, 4 \cdot \pi] \tag{34}$$

The rotation angle φ_1 will be assigned arbitrary values belonging to the range specified by the relationship (34). These values must cover the entire range. Their calculation formula is specified below:

$$\varphi_{1,i} = \left[(i-1)/n\right] \cdot (4 \cdot \pi) \tag{35}$$

In the relation (35) the values of the natural number "i" belong to the following interval:

$$i \in [1,\, n+1] \tag{36}$$

Each value of the φ_1 angle corresponds to a single value of the φ_2 angle:

$$\varphi_{2,i} = -\arcsin\left[\left(l_1/l_2\right) \cdot \sin\varphi_{1,i}\right] \tag{37}$$

The x_{O_2} abscissa values are given by the following relationship:

$$x_{O_2,i} = l_1 \cdot \cos\varphi_{1,i} \tag{38}$$

The y_{O_2} ordinate values will be calculated using the following relation:

$$y_{O_2,i} = l_1 \cdot \sin\varphi_{1,i} \tag{39}$$

The x_{O_3} abscissa values are given by the following relationship:

$$x_{O_3,i} = l_1 \cdot \cos\varphi_{1,i} + l_2 \cdot \sqrt{1 - \left(l_1/l_2\right)^2 \cdot \left(\sin\varphi_{1,i}\right)^2} \tag{40}$$

The y_{O_3} ordinate values will be calculated using the following relation:

$$y_{O_3,i} = 0 \tag{41}$$

It may be observed that the calculus depends on the values of the natural number "n". The natural number "n" must be as large as possible if the results obtained are to be very precise. Further on, the same kinematical study will be performed but this time the incremental numerical method will be used. The following relationship will be used for calculating the $\Delta\varphi_1$ increment:

$$\Delta\varphi_1 = \varphi_{1,n+1}/n = \left[(i-1)/n\right] \cdot (4 \cdot \pi)/n = 4 \cdot \pi/n \tag{42}$$

Performing a kinematical study is not possible unless the initial configuration of the mechanism is known first. For this, the position of each element of the mechanism must be known. Therefore, it will be assumed that the initial value of the φ_1^* angle is known and the kinematical parameters of the other elements of the mechanism will be expressed according to it. In order to do this the relationships (6-10) will be used:

$$x_{O_2}^* = l_1 \cdot \cos\varphi_1^* \tag{43}$$

$$y^*_{O_2} = l_1 \cdot \sin\varphi_1^* \quad (44)$$

$$\varphi_2^* = -\arcsin\left[(l_1/l_2)\cdot\sin\varphi_1^*\right] \quad (45)$$

$$x^*_{O_3} = l_1\cdot\cos\varphi_1^* + l_2\cdot\sqrt{1-(l_1/l_2)^2\cdot(\sin\varphi_1^*)^2} \quad (46)$$

$$y_{O_3} = l_1\cdot\sin\varphi_1 - l_1\cdot\sin\varphi_1 = 0 \quad (47)$$

Performing these laborious calculations was possible only with the help of a computer. That's why a MATLAB program was developed. The algorithm underlying the program is based on formulas (29-33). The program uses the following input data:

$$l_1 = 1\,[meters] \quad (48)$$

$$l_2 = 4\,[meters] \quad (49)$$

The initial position of the mechanism is given by the following positional parameters:

$$\varphi_1^* = 0\,[radians] \quad (50)$$

$$x^*_{O_2} = l_1\cdot\cos\varphi_1^* = l_1 = 1\,[meters] \quad (51)$$

$$y^*_{O_2} = l_1\cdot\sin\varphi_1^* = 0\,[meters] \quad (52)$$

$$\varphi_2^* = -\arcsin\left[(l_1/l_2)\cdot\sin\varphi_1^*\right] = 0\,[radians] \quad (53)$$

$$x^*_{O_3} = l_1\cdot\cos\varphi_1^* + l_2\cdot\cos\varphi_2^* = 5\,[meters] \quad (54)$$

$$y^*_{O_3} = l_1\cdot\sin\varphi_1^* + l_2\cdot\sin\varphi_2^* = 0\,[meters] \quad (55)$$

The coefficients of the algebraic system (24) will be recalculated for the next increment of time as follows:

$$\varphi_1^*(t_{i+1}) = \varphi_1^*(t_i) + \Delta\varphi_1(t_{i+1}) \quad (56)$$

$$\varphi_2^*(t_{i+1}) = \varphi_2^*(t_i) + \Delta\varphi_2(t_{i+1}) \quad (57)$$

The values of the small but finite variations $\Delta\varphi_1$ and $\Delta\varphi_2$ will be calculated using the relations (42) and (31). The values of the coordinates $x^*_{O_2}$, $y^*_{O_2}$, $x^*_{O_3}$ and $y^*_{O_3}$ will be calculated again for every increment of time as follows:

$$x^*_{O_2}(t_{i+1}) = x^*_{O_2}(t_i) + \Delta x_{O_2}(t_{i+1})\,[meters] \quad (58)$$

$$y^*_{O_2}(t_{i+1}) = y^*_{O_2}(t_i) + \Delta y_{O_2}(t_{i+1})\,[meters] \quad (59)$$

$$x^*_{O_3}(t_{i+1}) = x^*_{O_3}(t_i) + \Delta x_{O_3}(t_{i+1})\,[meters] \quad (60)$$

$$y^*_{O_3}(t_{i+1}) = y^*_{O_3}(t_i) + \Delta y_{O_3}(t_{i+1})\,[meters] \quad (61)$$

The values of Δx_{O_2}, Δy_{O_2}, Δx_{O_3} and Δy_{O_3} will be calculated using the relations (29), (30), (32) and (33) as follows:

$$\Delta x_{O_2}(t_{i+1}) = -l_1\cdot\sin\varphi_1^*(t_i)\cdot\Delta\varphi_1(t_{i+1}) \quad (62)$$

$$\Delta y_{O_2}(t_{i+1}) = l_1\cdot\cos\varphi_1^*(t_i)\cdot\Delta\varphi_1(t_{i+1}) \quad (63)$$

$$\Delta\varphi_2(t_{i+1}) = -(l_1/l_2)\cdot\left[\cos\varphi_1^*(t_i)/\cos\varphi_2^*(t_i)\right]\cdot\Delta\varphi_1(t_{i+1}) \quad (64)$$

$$\Delta x_{O_3} = l_1\cdot\left[\sin(\varphi_2^*(t_i)-\varphi_1^*(t_i))/\cos\varphi_2^*\right]\cdot\Delta\varphi_1 \quad (65)$$

$$\Delta y_{O_3} = 0 \quad (66)$$

The increment of time Δt is determined using the following formula:

$$\Delta t = t_{i+1} - t_i \quad (67)$$

The results are presented in the figures below (Fig.2-Fig.6):

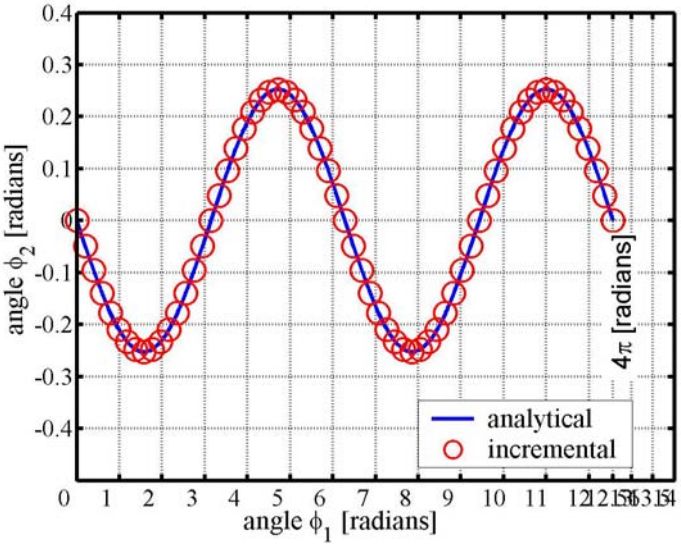

Figure 2. Variation of φ_2 angle as a function of φ_1 angle

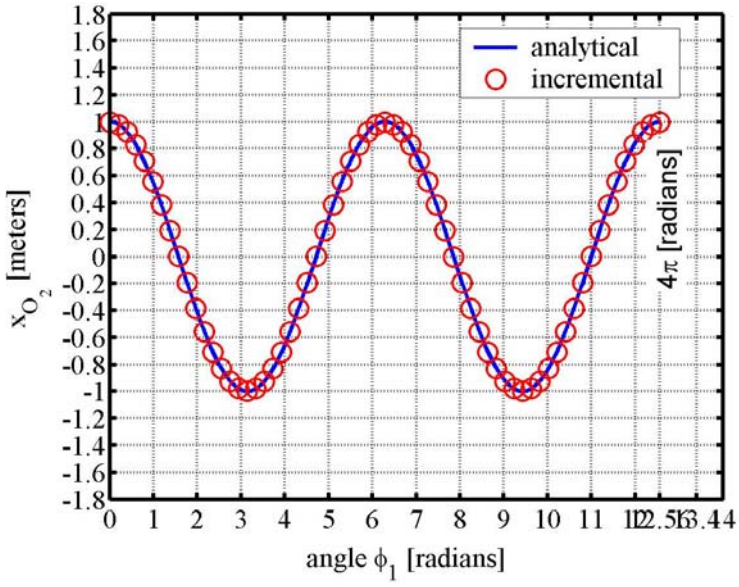

Figure 3. Variation of x_{O_2} abscissa as a function of φ_1 angle

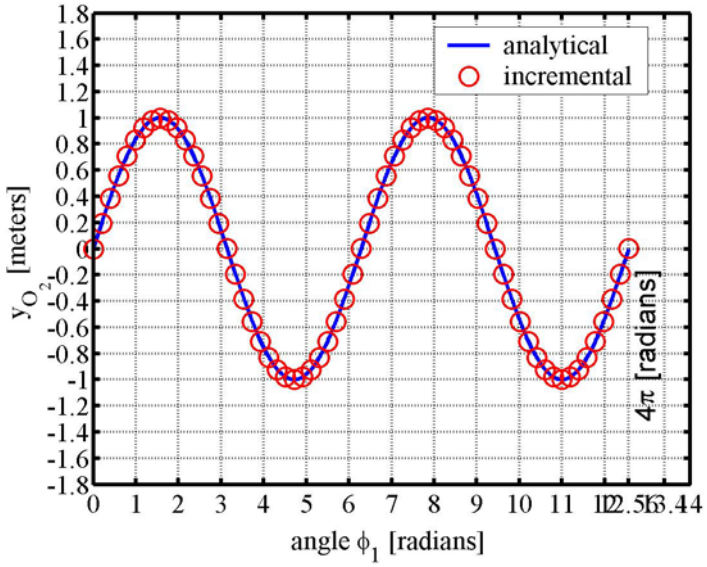

Figure 4. Variation of y_{O_2} ordinate as a function of φ_1 angle

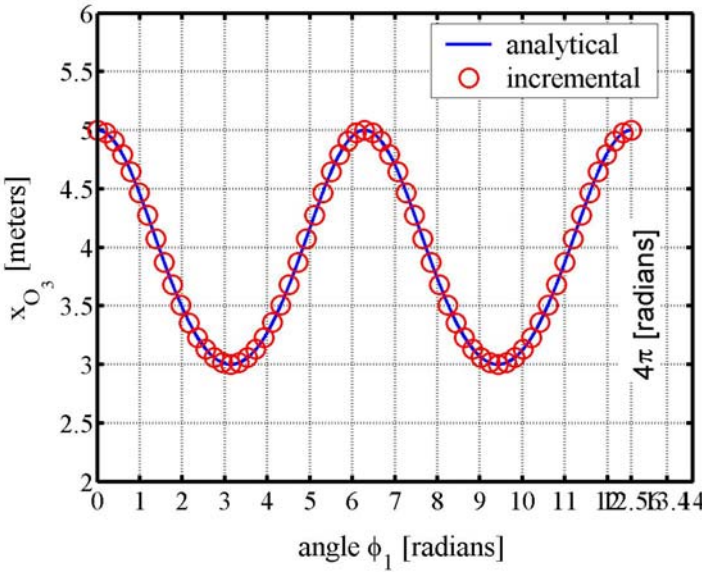

Figure 5. Variation of x_{O_3} abscissa as a function of φ_1 angle

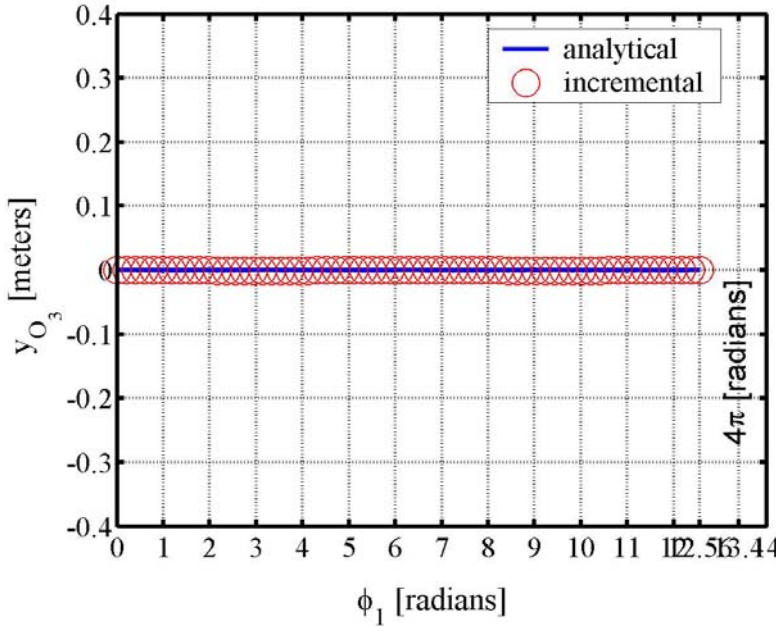

Figure 6. Variation of y_{O_3} ordinate as a function of φ_1 angle

The above figures (Fig.2-Fig.6) represent the variation of the position parameters of the mechanism elements as a function of the φ_1 angle values. Angle φ_1 represents the position parameter of the leading element.

5. CONCLUSIONS

An original numerical method has been presented in the paper. The originality of this work consists in transforming a system of differential equations into a system of algebraic equations. This was possible by moving from infinitely displacements (linear or angular) to finite but small displacements. In this way a system of algebraic equations with constant coefficients over an increment of time was obtained. The values of these coefficients was recalculated for the next step on the direction of time. In order to validate the numerical incremental method, a numerical example was presented.

6. REFERENCES

[1] Vâlcovici V., Bălan Şt., Voinea R., Mecanica Teoretică, Bucureşti, Editura Tehnică, 1968

[2] Viorel Handra Luca, Ion Aurel Stoica, Introducere in teoria mecanismelor, vol.I, Editura Dacia Cluj-Napoca, 1982, pp. 94-97

[3] Christian Pelecudi, Dezideriu Maros, Vasile Merticaru, Nicolae Pandrea, Ion Simionescu, Mecanisme, Editura Tehnica Bucuresti, 1983, pp.206-208

[4] Ştefan Staicu, Mecanica Teoretică, Bucureşti, Editura Didactică şi Pedagogică R.A., 1998

[5] Florin Bauşic, Mecanica Teoretică. Cinematica., Bucureşti, Editura Conspress, 2004

[6] Staicu Şt., Kinematics of translation-rotation hybrid parallel robot, Romanian Journal of Technical Sciences-Applied Mechanics, 60, pp. 171-183, 2015

[7] Staicu Şt., Dynamics modeling of a Stewart-based hybrid parallel robot, Advanced Robotics, 29, 14, pp.929-938, 2015

[8] Staicu Şt., Dynamics of the spherical 3-UPS/S parallel mechanism with prismatic actuators, Multibody Systems Dynamics, 22, 2, pp.115-132, 2009

[9] Voinea R., Stroe I., A general method for kinematics pairs synthesis, Mechanism and Machine Theory, Elsevier 30, 2, pp.461-470, 1995

[10] Staicu S., Zhang D., A novel dynamic modeling approach for parallel mechanisms analysis, Robotics and Computer-Integrated Manufacturing, Elsevier 21, 1, pp.167-172, 2008

[11] Staicu S., Liu X-J., Li J., Explicit dynamics equations of the constraint robotics systems, Nonlinear Dynamics, Springer 58, 1-2, pp.217-235, 2009

[12] Staicu S., Dynamics of a 2-DOF orienting gear mechanism, Rev. Roum. Sci. Techn., 5, 1, pp.67-77, 2009

[13] Stroe I., Staicu S., Calculus of joint forces using Lagrange equations and principle of virtual work, Proceedings of the Romanian Academy, Series A, 11,3, pp.253-260, 2010

[14] Staicu S., Matrix modeling of inverse dynamics of spatial and planar parallel robots, Multibody System Dynamics, 27, 2, pp.239-265, 2012

[15] Li Y., Staicu S., Inverse dynamics of a 3-PRC parallel kinematic machine, Nonlinear Dynamics, 67, 2, pp.1031-1041, 2012

[16] Stefan S, Andrei C., Inverse dynamics of translation-rotation hybrid parallel robot, Romanian Journal of Technical Sciences-Applied mechanics, vol.62 N°1, pp.47-56, Bucharest 2017